Ice properties of single-layer stratocumulus during the Mixed-Phase Arctic Cloud Experiment: 1. Observations

Greg M. McFarquhar,[1] Gong Zhang,[1] Michael R. Poellot,[2] Gregory L. Kok,[3] Robert McCoy,[4] Tim Tooman,[4] Ann Fridlind,[5] and Andrew J. Heymsfield[6]

Received 7 March 2007; revised 10 July 2007; accepted 8 August 2007; published 20 December 2007.

[1] During the Department of Energy's Atmospheric Radiation Measurement Program's Mixed-Phase Arctic Cloud Experiment (M-PACE) in fall 2004, the University of North Dakota Citation measured 53 profiles within single-layer stratus clouds by executing spiral ascents and descents over Barrow and Oliktok Point, Alaska, and by flying ramped ascents and descents between. Cloud phase was identified from an algorithm that uses voltage change from the Rosemount ice detector, the size distribution (SD) shape measured by the Forward Scattering Spectrometer Probe (FSSP), and manual identification of particles imaged by the Cloud Particle Imager, the two-dimensional cloud probe (2DC) and the high-volume precipitation sampler (HVPS). Size and mass distribution functions were derived using data from the FSSP, one-dimensional cloud probe, 2DC and HVPS in conjunction with total water content (TWC) measured by the Counterflow Virtual Impactor. With clouds defined as locations where TWC > 0.001 g m^{-3}, there were a total of 513 30-s averaged SDs in single-layer clouds, of which 71% were in mixed-phase parcels, 23% in ice-phase and 6% in liquid-phase. The mixed-phase parcels were dominated by contributions from liquid drops, with the liquid mass fraction f_l having averages and standard deviations of 0.89 ± 0.18 with 75% of cases having $f_l > 0.9$. For these single-layer clouds, f_l increased with normalized cloud altitude z_n, defined as linearly increasing from 0 at cloud base to 1 at cloud top with f_l averaging 0.96 ± 0.13 near $z_n = 1$ and 0.70 ± 0.30 near $z_n = 0$. The effective radius of water droplets r_{ew} increased with z_n, from an average of 6.9 ± 1.8 μm near $z_n = 0$ to 11.4 ± 2.4 μm near $z_n = 1$, whereas the effective radius of ice crystals r_{ei} (25.2 ± 3.9 μm) was nearly independent of z_n. The averaged cloud droplet number concentration and concentrations of ice crystals with maximum dimensions greater than 53 μm were 43.6 ± 30.5 × 10^3 L^{-1} and 2.8 ± 6.9 L^{-1}, respectively, and nearly independent of z_n. In contrast to past measurements in mixed-phase clouds combined from many geographical locations where f_l increased with temperature, f_l decreased from −12° to −3°C as clouds typically consisted of a liquid topped layer with precipitating ice below.

Citation: McFarquhar, G. M., G. Zhang, M. R. Poellot, G. L. Kok, R. McCoy, T. Tooman, A. Fridlind, and A. J. Heymsfield (2007), Ice properties of single-layer stratocumulus during the Mixed-Phase Arctic Cloud Experiment: 1. Observations, *J. Geophys. Res.*, *112*, D24201, doi:10.1029/2007JD008633.

1. Introduction

[2] Large atmospheric, oceanic and terrestrial changes are occurring in the Arctic [*Vorosmarty et al.*, 2002] yet complex interactions between sea ice, snow cover, clouds, the ocean and atmosphere are not well understood. Such interactions must be better characterized before disagreements between general circulation model (GCM) simulations [e.g., *Lane et al.*, 2001] can be reduced, and predictions of climate change refined. Unlike clouds in other regions, arctic clouds have a net warming effect on the surface over the course of a year [*Zhang et al.*, 1996; *Walsh and Chapman*, 1998; *Intrieri et al.*, 2002b]. Further, the surface energy budget is sensitive to cloud properties. *Curry and Ebert* [1992] showed that the energy received at the surface could vary by 50 W m^{-2} when the effective radius of liquid cloud drops r_{ew} was changed by 50%, and *Harrington and Olsson* [2001] showed changes of up to

[1]Department of Atmospheric Sciences, University of Illinois, Urbana, Illinois, USA.
[2]Department of Atmospheric Sciences, University of North Dakota, Grand Forks, North Dakota, USA.
[3]Droplet Measurement Technologies, Boulder, Colorado, USA.
[4]Sandia National Laboratories, Livermore, California, USA.
[5]NASA Goddard Institute for Space Studies, New York, New York, USA.
[6]National Center for Atmospheric Research, Boulder, Colorado, USA.

0148-0227/07/2007JD008633

80 W m^{-2} due to changes in the effective radius of ice crystals r_{ei}. *Ebert and Curry* [1993] also showed that the equilibrium sea ice thickness was sensitive to changes in downward longwave and shortwave radiative fluxes that depend on cloud properties.

[3] Retrieval techniques for all-ice and all-liquid clouds during the Surface Heat Budget of the Arctic Experiment (SHEBA [*Curry et al.*, 2000]) could be used only 34% of the time, suggesting mixed-phase or overlapping clouds were present at other times [*Shupe et al.*, 2001]. Mixed-phase clouds are prevalent in arctic transition seasons [*Intrieri et al.*, 2002a], especially during the fall over Barrow at the Atmospheric Radiation Measurement (ARM) Program's North Slope of Alaska (NSA) site [*Wang et al.*, 2005; *Shupe et al.*, 2005]. These clouds are radiatively significant [*Dong et al.*, 2001; *Dong and Mace*, 2003; *Zuidema et al.*, 2005] and hence important for cloud feedbacks on other processes.

[4] *Hobbs and Rangno* [1998] showed that many arctic mixed-phase clouds have liquid tops precipitating ice, yet persist for long periods of time. Modeling studies suggest that they persist because of a balance between cloud top radiative cooling, microphysical heating, ice sedimentation and large-scale forcing [*Pinto*, 1998; *Harrington et al.*, 1999], a balance that depends on assumptions about ice crystal fall speeds, concentrations of ice nuclei, primary and secondary ice nucleation mechanisms and large-scale forcings [e.g., *Jiang et al.*, 2000; *Harrington and Olsson*, 2001; *Lohmann*, 2002; *Morrison et al.*, 2003].

[5] To evaluate model simulations and to develop model parameterization schemes for terminal fall speeds [e.g., *Heymsfield et al.*, 2002] and single-scattering properties [e.g., *McFarquhar and Cober*, 2004], observations of size, shape and phase distributions of hydrometeors are required. These distributions are also used to evaluate model assumptions about ice nucleation mechanisms, terminal fall speeds and riming collection efficiencies [e.g., *Harrington et al.*, 1999; *Girard and Curry*, 2001; *Khvorostyanov et al.*, 2001; *Morrison et al.*, 2003, 2005a, 2005b; *Carrio et al.*, 2005]. Observations of ice crystal shapes [e.g., *Korolev et al.*, 1999] and effective sizes [e.g., *Boudala et al.*, 2002], and of water droplet concentrations and sizes [e.g., *Tsay and Jayaweera*, 1984] are also critical for determining how clouds impact radiation [*Zhang et al.*, 1996] and for developing and evaluating remote sensing retrieval schemes [*Platnick et al.*, 2001; *Hobbs et al.*, 2001; *Frisch et al.*, 2002; *Shupe et al.*, 2005; *Hogan et al.*, 2006].

[6] GCM simulations are sensitive to the manner in which the fraction of liquid water (f_l = LWC/TWC, where LWC is the liquid water content) is parameterized as a function of temperature. *Gregory and Morris* [1996] and *Li and Le Treut* [1992] showed modeled fields changed significantly depending on the temperatures over which mixed-phase clouds were assumed to exist. *Smith* [1990], *Moss and Johnson* [1994], *Bower et al.* [1996] and *Boudala et al.* [2004] have all developed relationships for f_l in terms of temperature (T) and/or total water content (TWC), but it is not known how well these schemes, based on observations in mixed-phase clouds from a variety of formation mechanisms and meteorological regimes, represent Arctic conditions.

[7] Recent observations of f_l in mixed-phase clouds [*Cober et al.*, 2001; *Korolev et al.*, 2003] on horizontal scales of 2 to 10 km show that the f_l frequency distribution is peaked at values close to 0 and 1, with values near 0.5 occurring infrequently. For arctic stratus, *Dong and Mace* [2003] and *Zuidema et al.* [2005] showed that liquid dominates the mass contents and hence the radiative properties. However, because the manner in which ice and water are partitioned has significant impacts on radiative transfer and on vertical profiles of cloud heating [*Sun and Shine*, 1994; *Rotstayn et al.*, 2000], even in arctic clouds [*McFarquhar and Cober*, 2004], further observations of the frequency distributions of f_l and of the microphysical structure of mixed-phase clouds are clearly needed.

[8] Prior in situ observations of arctic mixed-phase clouds have shown liquid-topped clouds with precipitating ice beneath [*Hobbs and Rangno*, 1998]. Further, *Lawson et al.* [2001] noted striking variability in hydrometeor fields on a horizontal scale of 10 km and a vertical scale of 100 m, and *Rangno and Hobbs* [2001] noted that high ice particle concentrations in supercooled clouds might be explained by the fragmentation of delicate ice and the shattering of some drops during freezing in free fall. Observations of mixed-phase clouds in other geographic regions include those of *Field et al.* [2004], *Fleishauer et al.* [2002], *Heymsfield* [1993] and *Borovikov et al.* [1963]. Cloud measurements collected during the September–October 2004 Mixed-Phase Arctic Cloud Experiment (M-PACE) [*Verlinde et al.*, 2007], when the University of North Dakota Citation flew nearly 100 vertical profiles through arctic boundary layer stratus, give the most complete set of observations on the vertical structure of arctic stratus thus far obtained. Of these profiles, the 53 flown through single-layer stratus clouds are analyzed in this paper. The dependence of ice water content (IWC), liquid water content (LWC), TWC, f_l, r_{ew}, r_{ei}, N_i and N_w on T and altitude (z) are determined and compared against a parameterization of *Boudala et al.* [2004] developed using a larger data set of mixed-phase clouds from a variety of locations.

2. Instrumentation and Data Processing

2.1. Available Instrumentation

[9] During M-PACE the University of North Dakota (UND) Citation was equipped with a Particle Measuring Systems (PMS) forward scattering spectrometer probe (FSSP) sizing particles with maximum dimension D (defined as maximum particle size in any direction) between 0.003 and 0.053 mm (3 to 53 μm), a PMS one-dimensional cloud probe (1DC) for $0.02 < D < 0.62$ mm, a PMS two-dimensional cloud probe (2DC), nominally for $0.03 < D < 0.96$ mm, and a high-volume precipitation sampler (HVPS) for $0.4 < D < 40$ mm. Data were acquired using a Science Engineering Associates data system. The size distributions (SDs) were calculated using software designed by William Hall at the National Center for Atmospheric Research and subsequently modified at Illinois [*McFarquhar et al.*, 2007a]. High-resolution (2.3 μm) particle images were acquired with a Cloud Particle Imager (CPI).

[10] The Citation was also equipped with a Counterflow Virtual Impactor (CVI) that provided bulk measures of TWC greater than 1 mg m^{-3} by evaporating particles with

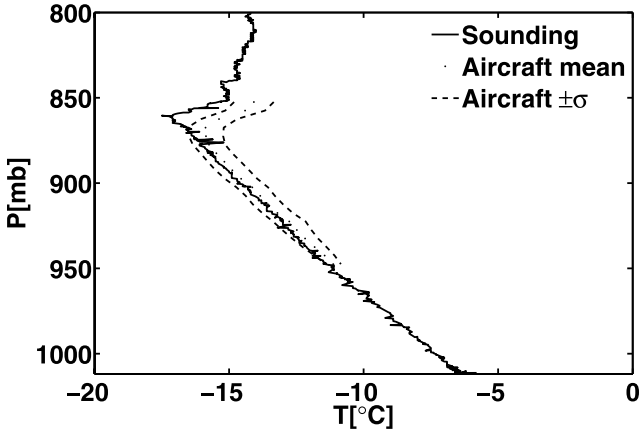

Figure 1. Mean T and P derived using aircraft temperature/pressure probes from spirals over Oliktok Point on 10 October between 2120 and 2250 UTC. Dashed line represents one standard deviation above and below the mean based on 8 spirals for which the temperature probe worked. Solid line represents profile measured by sounding released from Oliktok Point at 2300 UTC.

D > 5 μm in dry air and measuring the resulting vapor using a tunable diode laser absorption hygrometer [*Twohy et al.*, 2003]. The CVI TWCs are estimated to have an accuracy of approximately 15% (G. Kok, personal communication, 2007). A hysteresis effect observed in cirrus measurements in past campaigns was not as much of a problem for M-PACE because of the higher pressures and TWC where the measurements were made. A Rosemount Icing Detector (RICE) detected the presence of supercooled water through voltage changes induced by water freezing on and changing a cylinder's vibration frequency. The King probe provides bulk measures of LWC within 15% [*King et al.*, 1985] and "responds partially to some ice particles" [*Feind et al.*, 2000], but this should have minimal impact on the measured LWCs because arctic mixed-phase clouds are mainly composed of water. Except for a flight on 9 October 2004 when the tunable diode laser on the CVI did not initialize and flights before 10 October 2004 when the HVPS did not record data, all microphysical probes worked well throughout the experiment.

[11] *Strapp et al.* [2003] showed that the King probe measured LWCs of between 70% and 45% of the actual value for median volume diameters between 50 and 200 μm during wind tunnel tests. *Twohy et al.* [2003] also showed that the CVI could underestimate LWC for mean volume diameters smaller than 30 μm. To assess probe performance and to determine if either probe misses more small droplets, the bulk LWC from the King probe and CVI were compared for times without significant drizzle or ice, defined as when no ice was seen in the 2DC and CPI images and 2DC concentrations were less than 0.1 l^{-1}. The average difference between the King probe and CVI was 7.2%, less than the measurement uncertainties. Further, for bulk LWC > 0.2 g m^{-3} (LWC < 0.2 g m^{-3}), the LWC calculated from the FSSP SDs was on average 25% (9%) and 29% (21%) less than that from the King probe and CVI, with the greater difference at higher LWCs possibly caused by coincident or dead-time loses on the FSSP.

[12] Other data collected by the Citation include the temperature measured by a Rosemount 102 total temperature sensor, the total pressure measured by a Rosemount 1201F1 probe and the altitude, latitude and longitude measured by an Applanix position and orientation system. A broken wire inside the pylon leading to the temperature probe could not be fixed during M-PACE, preventing it from properly deicing. Hence observations of T were unreliable for later parts of flights. For 11.1 hours of flight time profiling single-layer and multilayer clouds, 6.1 hours of T data, corresponding to 64 of the 99 profiles could not be recovered. Of the 99 profiles, 53 were flown through single-layer stratus.

[13] Temperature (T) data were available from at least one spiral on each date. Thus relationships between pressure (P) and T derived from early parts of flights could be applied to estimate T in later parts of flights. Figure 1 shows the mean and standard deviation (σ) of T as a function of P using data from 8 spirals over Oliktok Point with useable T data on the second 10 October flight. The σ of T averaged over all height levels was 0.6°C with a maximum of 0.7°C, showing that the variation in T between spirals on a given day at a specific location was comparable to the 0.5°C accuracy of the probe. The solid line represents the sounding released on 10 October 2300 GMT over Oliktok Point. With the exception of a 1.2°C difference between the rawinsonde and aircraft T at 868 mbar caused by an 8 mbar difference in the inversion height, differences are less than the 0.5°C accuracy of the probe. For spirals conducted over Barrow on 9 October between 2155 and 2207 UTC and on 10 October between 0108 and 0159 UTC, no T data were obtained by the Citation. Hence relationships between P and T derived from soundings released at Barrow at 2300 UTC were used to predict T at the aircraft location.

2.2. Phase, Size, and Habit Distributions

[14] Data from all in-cloud penetrations were analyzed to identify cloud phase and SDs using techniques based on *Cober et al.* [2001] and *McFarquhar and Cober* [2004]. Figure 2 summarizes the algorithm used to identify phase as ice, liquid or mixed, where mixed-phase means both ice and liquid were detected in the same 30-s interval, corresponding to horizontal distances of approximately 2.5 km and vertical distances <100 m. Information used by the algorithm include the following: the magnitude of the voltage change observed by the RICE, where voltage changes of 2 mV s^{-1} correspond to supercooled water [*Cober et al.*, 2001]; visual inspection of particle images from the 2DC, HVPS and CPI where nonspherical particles correspond to ice; and the shape of the FSSP SD, where a strongly peaked distribution between 5 and 20 μm corresponds to water droplets and a broader distribution to ice [*McFarquhar and Cober*, 2004]. For times corresponding to the vertical profiling of single-layer boundary layer clouds discussed here, 71% of the 30-s averaged cloud observations with TWC > 0.001 g m^{-3} were mixed-phase, 23% ice-phase and 6% liquid-phase. When defining cloud as points where TWC > 0.005 g m^{-3}, 74% of the distributions were mixed-phase, 20% ice-phase and 6% liquid-phase, representing only a minor difference.

[15] The FSSP, 1DC, 2DC and HVPS gave SDs over a continuous range of sizes. Particles smaller than 0.125 mm

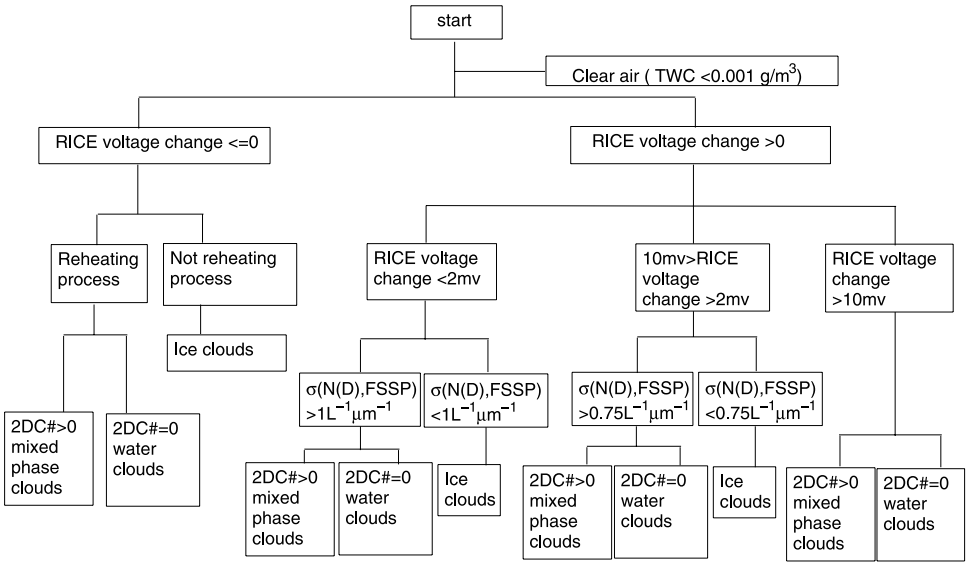

Figure 2. Algorithm used to identify the phase (ice-, liquid- or mixed-phase cloud) of each 30-s period of in situ data. Images from CPI, HVPS and 2DC were manually inspected for each 30-s period to reconfirm classifications or to further segregate water clouds into drizzle and nondrizzle cases.

measured by the 2DC are not used in this study because previous studies have suggested there are problems quantifying their concentrations with the 2DC [*Baumgardner and Korolev*, 1997; *Strapp et al.*, 2001]. For the overlap region of 1.3 to 1.5 mm where both the 2DC and HVPS registered enough counts to give 10% uncertainty in the number distribution function N(D), N(D) for the HVPS agreed within 69% of the 2DC. For flights before 10 October when the HVPS did not work, particles with D > 1.3 mm needed to be included in the SDs for accurate estimates of TWC. Using the average SD measured by the 2DC and HVPS on 12 October, Figure 3 shows the normalized cumulative mass distribution as a function of D. Crystals with D > 1.3 mm contributed 92% and 89% to the calculated TWC using mass calculation techniques of *Brown and Francis* [1995] and *Heymsfield et al.* [2002], respectively. Appendix A describes a technique for including crystals with D > 1.3 mm in the SDs when HVPS data are not available by extending fits to the 2DC SDs to larger sizes.

[16] The 2DC and HVPS data were computed at 10-s resolution, but subsequently averaged to 30-s to ensure adequate statistical sampling while still allowing reasonable temporal resolution. Following *Hallett* [2003], Figure 4

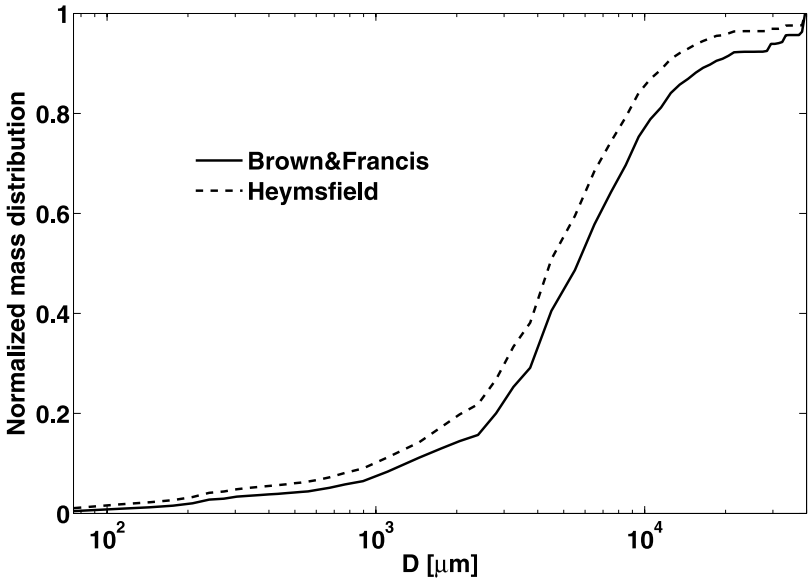

Figure 3. Normalized mass distribution function as a function of D for average SD measured on 12 October using 2DC and HVPS data. Line types in legend give m-D [*Brown and Francis*, 1995] or m-D-AR [*Heymsfield et al.*, 2002] relation used to calculate mass from measured crystals.

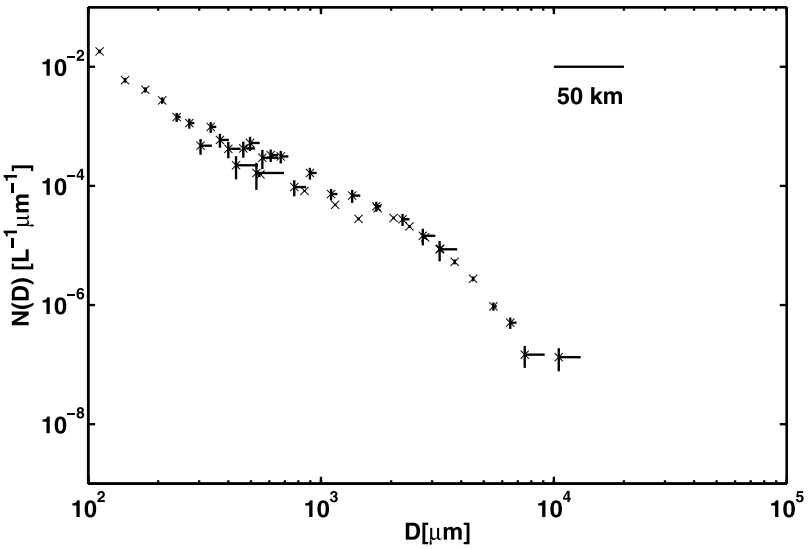

Figure 4. N(D) measured by 2DC (D < 1.3 mm) and by HVPS (D > 1.3 mm) against D for size distribution averaged over all time periods in cloud for 10 October. Vertical error bars represent uncertainty in N(D), where lines run between N(D) calculated using $N \pm N^{1/2}$ where N is the average number of particles measured in each size bin over 30-s period. Horizontal bars represent distance that UND Citation would have to travel to get 10% uncertainty in derived N(D), that is to sample 100 particles in the given size bin (horizontal axis corresponding to distance embedded in top right part of figure).

shows uncertainties in N(D) for a 30-s SD and the distance the Citations would have had to travel to sample 100 ± 10 particles in each size bin near the cloud base of 900 m for the 10 October flight at 223900 UTC. The FSSP and 1DC distributions were analyzed at 10-s resolution because there was adequate statistical sampling at this resolution. The methodology for deriving the number distribution function of water drops, $N_w(D)$, and of ice crystals, $N_i(D)$ from the FSSP, 1DC, 2DC and HVPS data is discussed below.

[17] For liquid phase clouds, the SDs of the FSSP (3 to 53 μm) were simply combined with those of the 1DC (53 to 125 μm), 2DC (125 to 1000 μm) and HVPS (1000 μm to 4 cm) to cover the complete particle size range. For mixed-phase clouds, particle morphology was used to identify size ranges that corresponded to ice crystals and water drops. The area ratio (AR), the projected area of a particle divided by the area of a circumscribed circle (equation (1)) [*McFarquhar and Heymsfield*, 1996], gives an indication of particle phase. Most liquid particles have AR > 0.8, but some ice crystals also have AR > 0.8 because of their shape or orientation when imaged. Thus the AR of an individual particle does not determine its phase. However, AR statistics can be used to suggest whether particles in specific size ranges are predominantly water or ice. For example, CPI images of particles with D > 0.125 mm have average AR of 0.45 ± 0.15 in ice-phase clouds and 0.48 ± 0.21 in mixed-phase clouds, with only 41 of 388 particles having AR > 0.8 in mixed-phase conditions. A Mann-Whitney U test shows that these mean AR are identical at a 93% confidence level. Hence particles with D > 0.125 mm were assumed to be ice consistent with *McFarquhar and Cober* [2004]. Because the supersaturation with respect to ice is higher than that with respect to water, it is reasonable that larger particles were ice that grew at the expense of supercooled drops.

[18] Figure 5 shows the average SDs measured in single-layer clouds in conditions identified as mixed-phase, ice-phase and liquid-phase. The HVPS curve includes contributions from the 2DC extensions for flights on 9 October and 10 October (first flight). Figure 5 shows that FSSP SDs under mixed-phase conditions peaked at D = 20 μm, just like the FSSP SDs in liquid-phase conditions. On the other hand, FSSP SDs for ice phase conditions did not exhibit these peaks and were flatter. These results indicate that the smaller particles in mixed-phase clouds were most likely supercooled water, which is the same as the *McFarquhar and Cober* [2004] study. Thus it was assumed that the mixed-phase FSSP SDs represented supercooled water droplets for 3 < D < 53 μm.

[19] To determine the phase of particles with D > 53 μm, a habit identification scheme was applied to the CPI images. Of the 285 30-s mixed-phase time periods, only 18% had at least a single particle between 0.053 < D < 0.125 mm that was clearly spherical and drizzle; only 19% had a particle between 0.053 < D < 0.512 mm that was drizzle. There were typically nonspherical particles between 0.053 < D < 0.125 mm, suggesting many particles in this size range were ice. When the morphology of the CPI images was examined, the AR of particles with 0.053 < D < 0.125 mm averaged 0.85 for the drizzle time periods compared to 0.75 for other periods. Thus 1DC particles with 0.053 < D < 0.125 mm were assumed to be ice when drizzle was not present; otherwise, they were assumed to be liquid drops.

[20] For ice clouds, the ability of the FSSP to measure ice crystal SDs has not been well established [*Gardiner and Hallett*, 1985; *Field et al.*, 2003; *McFarquhar et al.*, 2007b] and there is some evidence that large ice crystals shatter on the protruding airflow shrouds of the FSSP generating artificially high counts of small crystals. The FSSP SDs for ice-phase conditions were flat in Figure 5, consistent

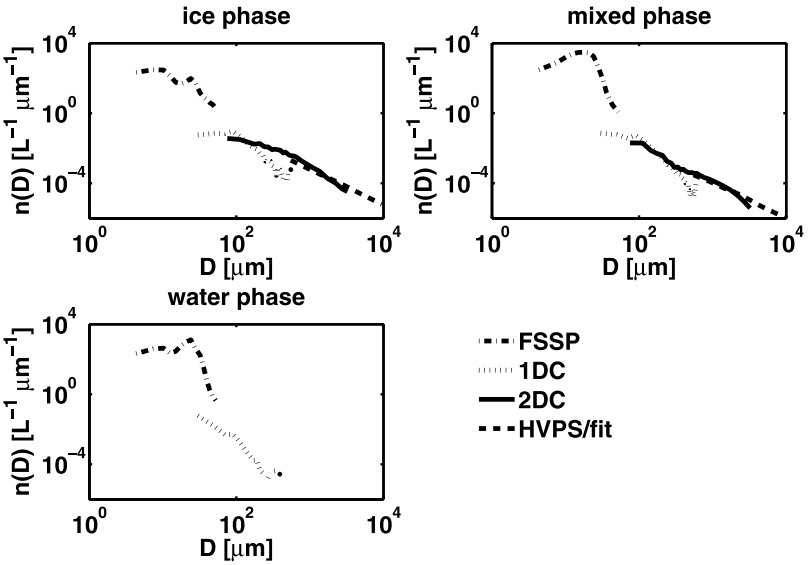

Figure 5. Average n(D) as function of D for all SDs measured in single-layer clouds for ice-phase, liquid-phase and mixed-phase conditions. Data are acquired from FSSP, 1DC, 2DC and HVPS as indicated in legend. For SDs measured on 9 October and the first 10 October flight, fits to 2DC data rather than HVPS data were used to characterize the curve labeled HVPS because HVPS data were missing on these dates.

with previous observations in ice. To account for the uncertainty in the SDs of small crystals, two different representations were used with the FSSP SD regarded as an upper bound [*McFarquhar et al.*, 2003] and a SD assuming N(D) = 0 for D < 53 μm regarded as a lower bound. *Field et al.* [2006] also showed that observations from two-dimensional probes could be affected by the shattering process with measured concentrations affected by up to a factor of 4 when mass-weighted mean sizes were larger than 3 mm and IWC overestimated by 20 to 30%. No explicit attempt has been made to correct for these effects here, but given that the bulk properties are obtained by matching the IWC derived from the SDs with that measured by the CVI (see section 3), there is an implicit consideration in calculation of bulk properties. The 1DC, 2DC and HVPS or extensions to the 2DC data were thus used to characterize the SDs of particles with D > 53 μm for ice-phase clouds.

2.3. Derived Bulk Parameters

[21] This section describes how the bulk properties of the liquid and ice components of clouds were determined. For both liquid-phase and mixed-phase clouds, the best estimate of the LWC was the value measured by the King probe. The total concentration of liquid drops, N_{Tw}, was the zeroeth moment of $N_w(D)$. The effective radius of water droplets, r_{ew}, was the third moment of $N_w(D)$ divided by the second moment.

[22] Calculations were more complex for bulk ice properties because ice crystals are not spherical. In mixed-phase clouds, the IWC could not be estimated as the difference between the CVI TWC and the King probe LWC. Since liquid typically dominates the mass of mixed-phase clouds [*Dong and Mace*, 2003; *McFarquhar and Cober*, 2004; *Zuidema et al.*, 2005], CVI TWC - King LWC thus represents a small difference between two large numbers and hence has large fractional uncertainty. In fact, this difference was negative for 2670 of the 7570 s during M-PACE. Further, the IWC estimated as CVI TWC - King LWC and the IWC estimated from $N_i(D)$ assuming varying mass-diameter relationships [*Locatelli and Hobbs*, 1974; *Brown and Francis*, 1995; *Mitchell*, 1996; *Heymsfield et al.*, 2002] were frequently 2 orders of magnitude different, probably because of the large uncertainty in CVI TWC–King LWC. In order to include all these points in the analysis, an alternate procedure for determining IWC was developed.

[23] The IWC was instead estimated by determining a and b coefficients minimizing the χ^2 difference between the CVI IWC and the IWC derived from $N_i(D)$, given by

$$IWC = \sum_{i=1}^{M} aD_i^b N_i(D_i)\Delta D_i \quad (1)$$

where D_i is the diameter of the ith size bin with width ΔD_i and there are M size bins in total. Only 30-s periods identified as ice were used to minimize χ^2 in equation (1) because the difference between the CVI TWC and King LWC in mixed-phase clouds is not a good estimate of IWC as explained above. The coefficients derived from the ice-phase conditions, namely $a = 1.07 \times 10^{-10}$ g $\mu m^{-1.7}$ and b = 1.7, were then applied to estimate the IWC in mixed-phase clouds as well, meaning that an implicit assumption was made that the mixture of ice particle habits and densities did not vary for ice and mixed-phase clouds. This assumption is reasonable to first order given that the average AR were statistically identical for ice and mixed-phase clouds. Particles with D < 0.125 mm were not used in the summation in equation (1) because a and b coefficients appropriate for crystals with D > 0.125 mm frequently give masses larger than those for spherical equivalent particles for D < 0.125 mm. Ignoring these particles is reasonable

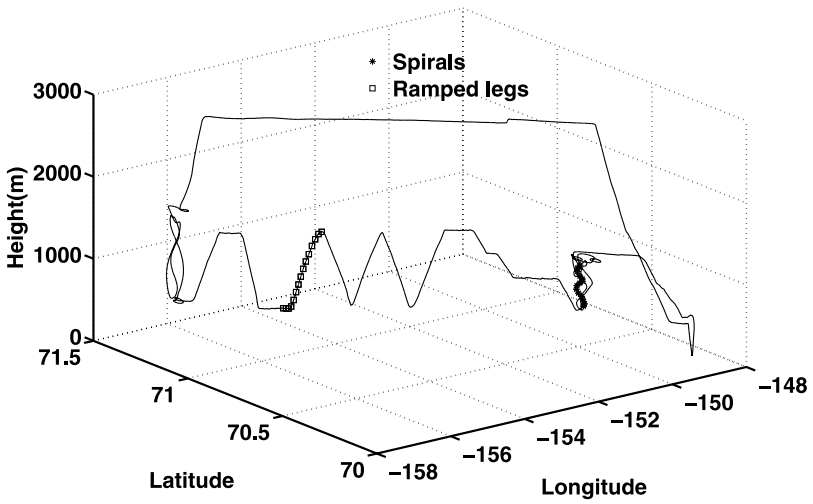

Figure 6. Flight track flown by the UND Citation on 9 October 2004 between 2010 and 2250 UTC. Location of ground-based remote sensing sites at Barrow and Oliktok Point are indicated by X and Y, respectively.

because they contribute at most 13% to the IWC when the upper bound of $N_i(D)$ and spherical particles are assumed for $D < 0.125$ mm.

[24] For both ice- and mixed-phase clouds, the total number of ice crystals, N_{Ti}, was estimated directly from $N_i(D)$. The cumulative cross-sectional area (A_c) for ice particles was given by

$$A_c = \sum_{i=1}^{M}\sum_{j=1}^{N}\frac{\pi}{4}AR_jD_i^2N\left(D_i, AR_j\right) \tag{2}$$

where AR_j corresponds to the area ratio of bin j and $N(D_i,AR_j)$ corresponds to the number distribution of ice crystals (L^{-1} bin^{-1}) in size bin i and area ratio bin j. The A_c is a direct measurement of projected area, or in the case of larger particles occurring on the edges of photodiodes, an estimate of the reconstructed area [*Heymsfield and Parrish*, 1978]. For the flight on 9 October and the first flight on 10 October when fits to 2DC data are extended to larger sizes, the average cross-sectional area of particles in size bin D_i was estimated as cD_i^b, where the c and b coefficients were derived using data acquired on the second flight of 10 October and from 12 October. The effective radius of ice crystals, r_{ei}, was defined following *Fu* [1996] and *McFarquhar and Heymsfield* [1998] as

$$r_{ei} = \frac{\sqrt{3}IWC}{3\rho_i A_c}, \tag{3}$$

where the bulk density of ice ρ_i was assumed to be 0.91 g cm^{-3}. For calculations in ice-phase clouds, two separate estimates of the bulk parameters were made using the lower and upper bound for contributions of crystals with $D <$ 0.053 mm.

3. Sampling Strategy

[25] The goal of M-PACE was to collect observations to advance the understanding of the dynamical, microphysical and radiative processes occurring in mixed-phase clouds [*Verlinde et al.*, 2007]. During M-PACE, spiral ascents and descents were flown through mixed-phase clouds by the UND Citation with the Scaled Composites Proteus aircraft sometimes remotely sensing cloud properties from above. Figure 6 shows a flight track flown by the UND Citation on 9 October 2004 between 2010 and 2250 UTC. After departing Prudhoe Bay (70°12′N, 148°28′W), the Citation ascended and descended through cloud in spirals over the ground-based remote sensing site at Oliktok Point (70°30′N, 148°53′W). The Citation then traveled about 300 km toward ARM's ground-based remote sensing site at Barrow (71°19′N, 156°37′W) performing both gradual ascents and descents between cloud top and base to sample vertical variability (hereafter called ramped legs), and constant altitude legs to sample horizontal variability [*Poellot and Brown*, 2006]. At Barrow, more spirals were performed before returning to Oliktok Point above cloud top to sample ice nuclei.

[26] Similar flight profiles were flown other days during M-PACE. The macrophysical properties of the clouds were different for flights conducted between 5 and 8 October compared to those conducted between 9 and 12 October. Ground-based remote sensors at Oliktok Point and Barrow showed that clouds typically occurred in a single vertically continuous layer for flights between 9 and 12 October, whereas multiple cloud layers were detected for flights conducted on and before 8 October. Figure 7 shows an example of the single-layer stratus sampled on 12 October using data collected by a cloud detection lidar on the Proteus as it flew 12 km high racetrack patterns over Barrow, a level leg between Barrow and Oliktok Point, and level racetracks over Oliktok Point in coordination with the Citation. The low-level clouds occurred beneath a clear sky extending to the tropopause and were optically thick as the lidar was occulted before reaching the ground. The strong inversion seen in Figure 1 likely capped the vertical development of these clouds.

[27] Table 1 lists the time periods, the averaged cloud top (z_t) and base (z_b) altitudes, and average cloud top (T_t) and

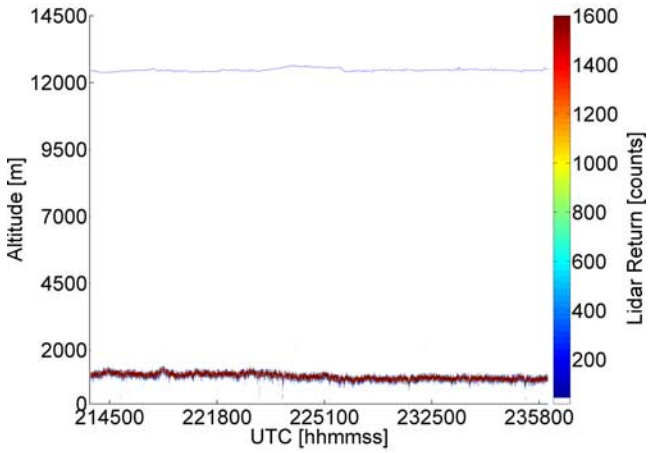

Figure 7. Backscatter intensity measured by cloud detection lidar on board Scaled Composites Proteus as it flew 12 km high racetrack patterns over Barrow (2138 to 2230 UTC), a straight line leg between Barrow and Oliktok Point (2230 to 2302 UTC) and racetrack patterns over Oliktok Point (2302 to 0001 UTC). Blue line above 12 km indicates position of Proteus; black line at 0 km indicates ground.

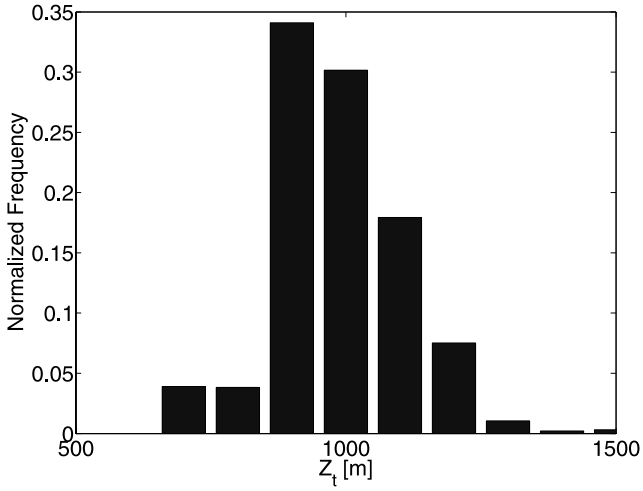

Figure 8. Normalized frequency distribution of z_t between 2130 and 0001 UTC on 12 October 2004, the time period included in Figure 6. The z_t were derived using *Wang and Sassen*'s [2001] algorithm.

base temperatures (T_b) for vertical profiles through single-layer stratus on 9 October, 10 October (2 flights) and 12 October, which includes 26 spirals over Oliktok Point, 10 over Barrow, and 17 ramped ascents and descents between the two sites. The z_b was determined from the ground-based lidar data at Oliktok Point or Barrow so that only precipitating ice was beneath z_b. For ramped ascents and descents, z_b was estimated as the lowest altitude where the FSSP had a strongly peaked SD, the peak corresponding to the nucleation of supercooled drops at cloud base. This gave an unambiguous z_b for all ramped ascents and descents. Precipitating ice was frequently noted below z_b.

[28] Because the lidar was typically occulted before reaching cloud top, z_t was defined as the altitude where the Citation ascended above cloud. The Citation failed to reach clear sky above cloud for only 2 of the 17 ramped legs. For those legs, z_t was assumed to be the same as the preceding leg. Both z_b and z_t were determined within 50 m, smaller than the variations caused by horizontal inhomogeneities discussed below.

[29] Two caveats are associated with the use of these data to represent vertical profiles of single-layer arctic clouds. First, not all profiles were flown from z_b to z_t because of air traffic control restrictions, or in some cases, the bases were too low to safely fly beneath. Second, the ramped legs covered approximately 22 ± 6 km of horizontal distance on average and the spirals had diameters of about 5 ± 3 km meaning cloud horizontal inhomogeneities complicated observed profiles. It is not known whether the inhomogeneities are the same at the 5 km and 22 km scales. To illustrate these inhomogeneities and the variability of z_t even on a single day, Figure 8 shows the normalized frequency distribution of z_t on 12 October determined using *Wang and Sassen*'s [2001] cloud boundary detection algorithm applied to the lidar data as shown in Figure 7. The z_t averages 1018 m with a standard deviation of 148 m. To illustrate the inhomogeneities of clouds during the first flight on 10 October, Figure 9 shows the frequency distribution of T_t determined from a pair of infrared thermometers on the Proteus. The averages and standard deviations of T_t were $-10.9° \pm 1.8°C$ and $-12.8° \pm 1.7°C$ derived from the 8 to 10 μm and 9.6 to 11.5 μm infrared measurements, temperatures for which mixed-phase clouds easily exist. Despite such inhomogeneities, the large number of spirals gives unprecedented information on the vertical structure of mixed-phase boundary layer clouds.

4. Observed Vertical Profiles

4.1. Overview

[30] In this section, the vertical variability of cloud properties is presented. Data from the second spiral on 10 October are first shown as an example of how cloud

Table 1. Start and Stop Times of All Spirals and Profiles Over and Between Barrow and Oliktok Point, Together With Average z_t, Average z_b, and the Average Cloud Top and Base Temperature

Date	Start, UTC	Stop, UTC	z_t, m	z_b, m	T_t, °C	T_b, °C
9 Oct	2020:10	2207:20	1238 ± 210	542 ± 98	−14.5 ± 1.3	−10.1 ± 0.1
10 Oct (a)	0010:10	0310:10	1154 ± 142	583 ± 111	−15.0 ± 1.3	−10.6 ± 0.9
10 Oct (b)	2130:30	2245:30	1322 ± 52	745 ± 50	−16.0 ± 0.8	−12.7 ± 0.4
12 Oct	2317:40	2359:30	885 ± 31	420 ± 29	−12.4 ± 1.3	−11.3 ± 0.2

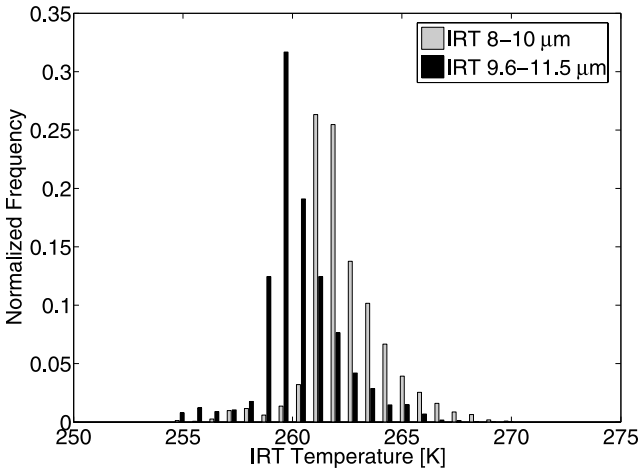

Figure 9. Normalized frequency distribution of cloud top temperature determined from pair of infrared thermometers (detection radiation in 8 to 10 μm and 9.6 to 11.5 μm bands) installed on Proteus. Observations acquired on 9 October 2003 between 1937 and 2220 UTC when the Proteus was flying in either racetrack patterns over Oliktok Point or Barrow or level leg in between.

habits, SDs and bulk parameters varied with altitude. Trends in how the bulk properties varied with normalized cloud altitude z_n, given by

$$z_n = \frac{z - z_b}{z_t - z_b}, \tag{4}$$

are summarized in the next subsection. The z_n was frequently negative because on many days observations were made in precipitating ice occurring below z_b. Differences noted between spirals conducted on different days and in different locations are assessed in the final subsection.

4.2. Variability Observed on Second Flight of 10 October

[31] The spiral conducted over Oliktok Point between 2140 and 2147 UTC on the second flight of 10 October is used to illustrate one of the profiles, which covered the range between z_b and z_t. The z_b and z_t were 750 m and 1300 m, estimated from the Pacific Northwest National Laboratory (PNNL) Active Remote Sensing Laboratory (PARSL) lidar and radar measurements, respectively. Figure 10 shows representative cloud particles imaged by the CPI, 2DC and HVPS during this spiral. Drizzle is seen near cloud top from the circular CPI images, but ice particles with irregular and rimed shapes are seen from the larger 2DC and HVPS images. Although the irregular large crystal images were more frequent near and below cloud base, they did occur through the cloud, indicating that water and ice coexisted on a relatively small spatial scale. The irregular shapes of ice crystals shapes as shown in Figure 10 are consistent with the study of *Korolev et al.* [1999].

[32] Figure 11 shows the SDs measured by the FSSP, 1DC, 2DC and HVPS for the same spiral as a function of height. The N(D) values represent 30-s averages for the 2DC and HVPS, and 10-s averages for the FSSP and 1DC. A peak 10^2 L^{-1} μm^{-1} of N(D) at D = 10 μm and 750 m height corresponds to z_b where drops were nucleated. The FSSP modal diameter increased with height to approximately 30 μm and N(D) increased up to 5×10^3 L^{-1} μm^{-1} near z_t where drops grew by condensation during ascent through the cloud. The strong peak in the FSSP N(D), together with the response of the RICE throughout the spiral (figure not shown), indicates that supercooled water was present

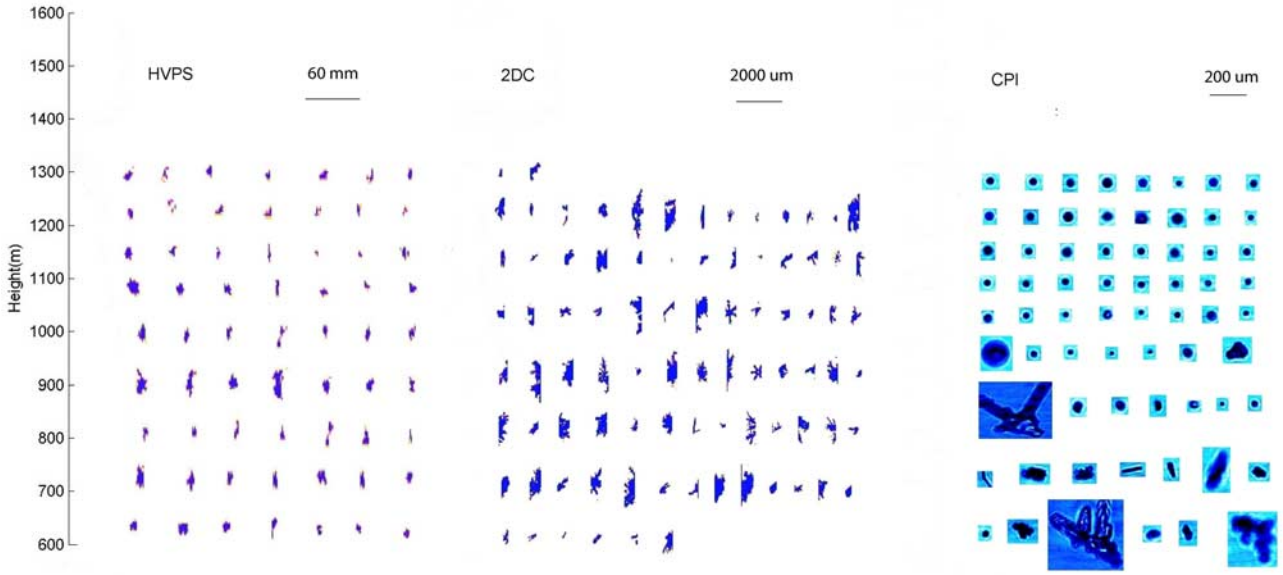

Figure 10. Example of selected (left) HVPS, (middle) 2DC and (right) CPI images acquired for spiral flown between 2140 and 2147 on 10 October 2004. Smaller spherical images near cloud top (CPI) are small drizzle or supercooled drops. Larger ice crystal images show dominance of irregular and rimed crystal shapes.

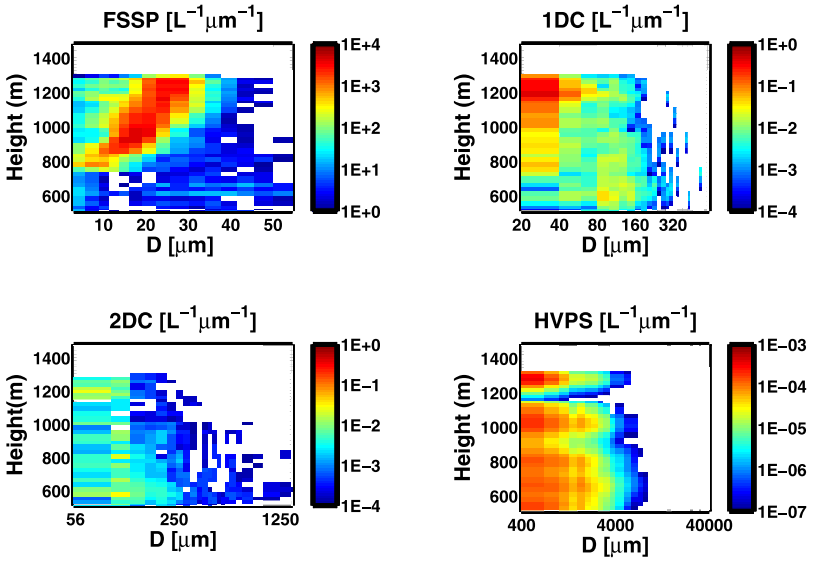

Figure 11. N(D) from FSSP ($3 < D < 53$ μm), 1DC ($20 < D < 640$ μm), 2DC ($100 < D < 1300$ μm) and HVPS ($D > 1300$ μm) as function of time and altitude for spiral over Oliktok Point between 2140 and 2147 UTC on 10 October 2004.

throughout this spiral. The 1DC registered high N(D) of 0.5 L^{-1} μm^{-1} for $20 < D < 40$ μm and N(D) up to 10^{-1} L^{-1} μm^{-1} for $40 < D < 60$ μm near z_t. Given the circular images with D of approximately 50 μm observed by the CPI near z_t, there is evidence that the collision-coalescence process may have occurred near cloud top producing drizzle.

[33] The nonzero N(D) of the 2DC and HVPS in Figure 11 correspond to the presence of ice as seen by the nonspherical crystals in Figure 10. The maximum D from the 2DC increased from 250 μm at 1300 m, to 800 μm at 1000 m and to nearly 1250 μm beneath cloud base at 600 m. The N(D) from the 2DC also increased with decreasing z with values of around 10^{-3} (0) L^{-1} μm^{-1} at 1300 m, 5×10^{-3} (10^{-4}) L^{-1} μm^{-1} at 1000 m and 10^{-2} (3×10^{-4}) L^{-1} μm^{-1} at cloud base around 800 m for D of 200 (1000) μm. Below cloud base, even larger N(D) of 5×10^{-2} (5×10^{-3}) L^{-1} μm^{-1} were observed at 600 m. This corresponds to precipitating ice as a flat signal from the FSSP and lack of response from the RICE, indicating that supercooled water was not present. For larger crystals measured by the HVPS N(D) values are smaller with a range of between 10^{-7} and 10^{-4} L^{-1} μm^{-1}. Although the HVPS concentrations are sharply reduced at altitudes near 900 and 1100 m compared to adjacent altitudes and although there may be a slight trend toward increasing particle sizes below cloud base, no strong altitude dependence is seen.

[34] Figure 12 shows how the bulk properties N_i, N_w, r_{ew}, r_{ei}, IWC, LWC and f_l varied with z for the spiral in Figure 11. The LWC increased with height while N_w remained a relatively constant value of 3×10^4 L^{-1} suggesting the supercooled droplets were nucleated near cloud base and then grew by condensation throughout the cloud. The r_{ew} increased with z, and values of 14 μm and modal diameters of 30 μm near z_t indicate that the collision-coalescence process was active. Although IWC varied throughout cloud, it increased with decreased z up to 0.005 g m^{-3} near z_b and to even larger values of 0.01 g m^{-3} corresponding to precipitating ice beneath z_b. The f_l had high values close to 1.0 throughout this cloud, but decreased to lower values beneath. These trends are consistent with the growth of cloud droplets during ascent and either the fallout of ice generated near the top or the generation of ice near the base. The supercooled cloud top temperatures of -16.9°C and low N_w of 3×10^4 L^{-1} correspond to the Type V conditions delineated by *Rangno and Hobbs* [2001], wherein ice number concentrations tend to exceed background ice nuclei concentrations. Ice formation under such conditions is further investigated using numerical modeling studies in Part 2 of this paper [*Fridlind et al.*, 2007].

[35] Diagrams similar to Figure 11 and Figure 12 were examined for the other profiles. In general, LWC increased from z_b to peak values between 0.3 and 0.5 g m^{-3} near z_t, the modal FSSP diameter and r_{ew} increased to values near 30 and 15 μm at z_t, and IWC was relatively invariant with z and had typical values around 0.01 g m^{-3}. However, there were differences between profiles that could not be easily explained with pockets of lower LWC noted on some profiles, and significant amounts of ice located near z_t on some legs, showing temporal and spatial inhomogeneities in cloud microphysical properties existed.

[36] There were also significant variations in cloud macrophysical properties between profiles. For example, for the ramped ascents and descents on 10 October (first flight), z_t ranged from 1020 m to about 1300 m near Oliktok Point, while the Citation did not reach that high near Barrow, and z_b values ranged from 480 to 550 m as well. On 10 October (first flight), z_t gradually increased from about 1250 m to 1400 m during the time the profiles were performed over Barrow. On the other hand, less variability was noted for profiles on 12 October over Oliktok point when z_b and z_t values were nearly constants at 420 m and 900 m, respectively. Thus, in order to better examine the microphysical variability between profiles a framework for plotting data from profiles with varying z_t and z_b was needed, namely

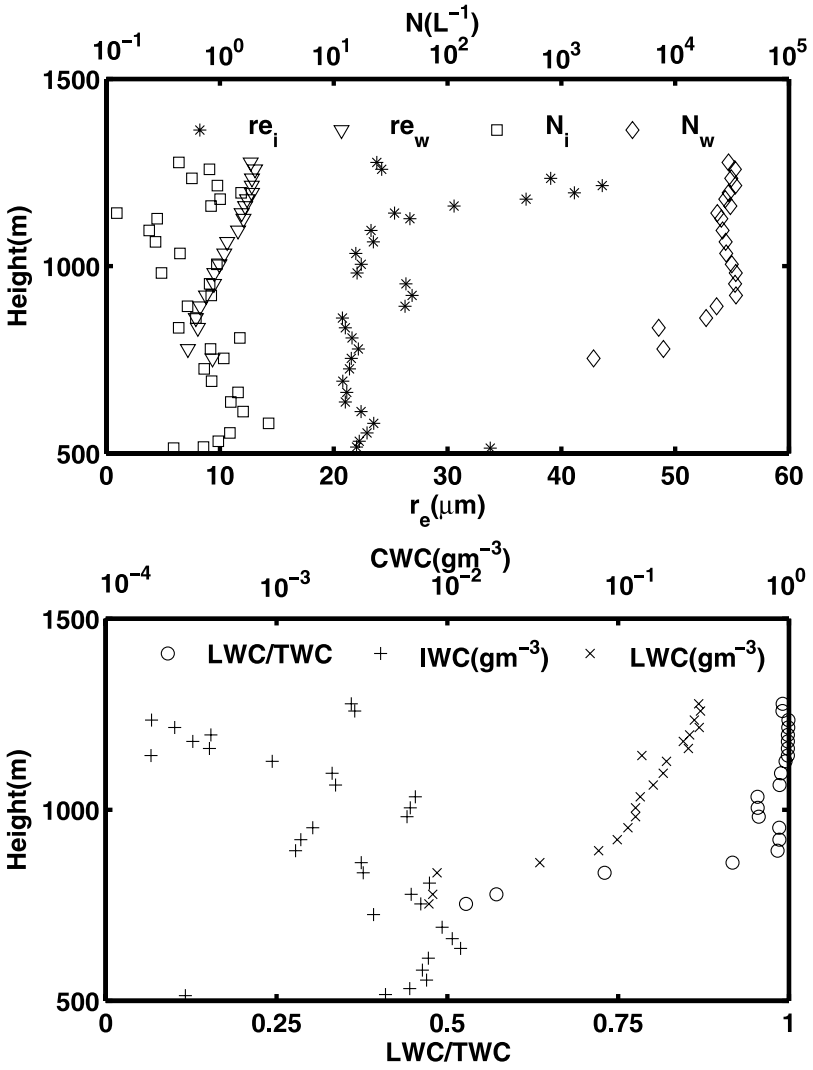

Figure 12. Bulk parameters as a function of height for the spiral on 10 October.

examining the dependence of microphysics properties as a function of z_n. This is considered in the next section.

4.3. Observed Trends in Vertical Variability of Bulk Parameter

[37] In addition to determining how bulk microphysical properties varied as a function of z_n, it was also necessary to determine if there were any trends in how the ice particle habits varied with z_n. An automated habit recognition scheme was applied to the CPI images, with hydrometeors classified as needles, columns, rosettes, semispheres, spheres or irregulars on the basis of measures of crystal morphology such as D, projected area and crystal perimeter. Figure 13 shows the normalized contribution of these habits to A_c as a function of z_n for all profiles through the single-layer boundary clouds. For the upper half of the cloud with $z_n > 0.5$, spherical and semispherical particles with $D < 60$ μm contributed 80% and 20%, respectively, to A_c, while other habits, that correspond to ice, contributed almost nothing to A_c. Thus, even if the semispheres were ice, the spheres corresponding to supercooled water dominated A_c, and hence the direct radiative impacts in the upper half of clouds. For $0 < z_n < 0.5$, spheres and semispheres made progressively smaller contributions to A_c with, for example, combined contributions of less than 60% at z_n of 0.2. Bullet rosettes and irregular ice crystals combined made up between 50 and 70% of the contributions to A_c near cloud base, showing that ice was becoming progressively more important in the bottom half of the cloud. It should also be noted that many of the crystals identified as rosettes could be more accurately described as rimed branched crystals because they did not resemble classical bullet rosettes.

[38] For the precipitating ice beneath cloud base where $z_n < 0$, rosettes and irregular crystals made almost 70% of the contributions to A_c. The 20% contributions from semispheres correspond to particles with $D < 120$ μm and are most likely quasi-spherical ice such as that described by *Nousiainen and McFarquhar* [2004]. Crystals with $D > 120$ μm dominate the contributions to A_c for $z_n < 0$. Thus the habit recognition scheme shows small circular particles dominated near cloud top and precipitating ice below cloud base, which is consistent with the *Hobbs and Rangno* [1998] study. Compared to the *Korolev et al.* [1999] study, who found irregular ice crystals represented about 98% of

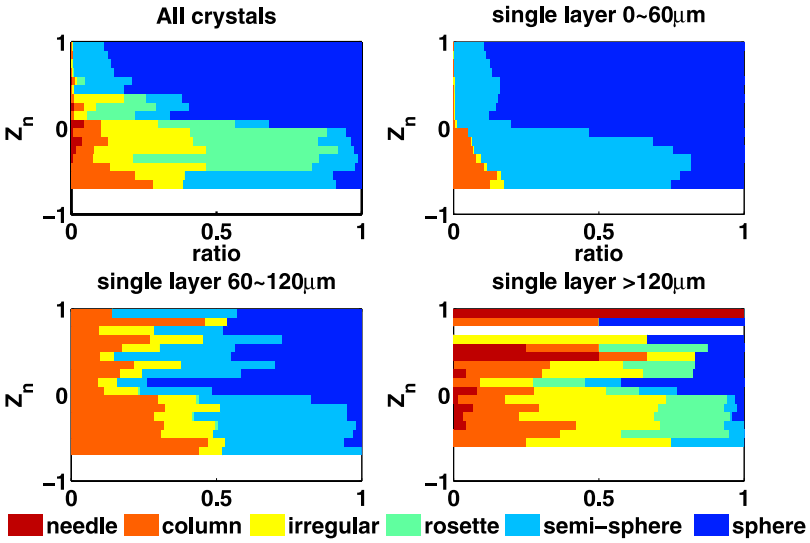

Figure 13. Normalized fractional contribution of different habits to the total measured cross-sectional area (A_c) as a function of z_n derived from all spirals flown through single-layer Arctic stratus on 9 October, 10 October and 12 October. Habit fractions derived from automated habit recognition scheme applied to CPI data, A_c derived from analysis of CPI images.

the images, Figure 13 shows more pristine crystals. Although the habit recognition scheme may have overestimated contributions from these pristine habits, visual analysis of CPI images showed that some bullet rosettes were indeed present.

[39] Analysis of other bulk variables shown in Figure 14 yielded trends consistent with single-layer liquid topped clouds precipitating ice. When defining clouds as locations where TWC > 0.005 g m^{-3} instead of where TWC > 0.001 g m^{-3} as in Figure 14, there were very minor quantitative differences and no differences in observed trends. Figure 14a shows how the liquid water fraction, f_l = LWC/(IWC+LWC), varied with z_n. For $z_n > 0.5$, f_l averaged 0.97 and for $0.0 < z_n < 0.5$, f_l gradually increased from 0.7 to 0.9. Liquid still dominated TWC on average for all $z_n > 0.0$. The curve fitting of f_l on z_n can be approximated by a second-order polynomial fit given by

$$f_l = 0.727 + 0.677 z_n - 0.443 z_n^2 \quad (5)$$

which is valid for the range $0 < z_n < 1$. However, there were a few specific clouds that deviated from the average represented by equation (5) with ice dominating near cloud base. Overall, the dominance of liquid water in arctic mixed-phase clouds is consistent with *McFarquhar and*

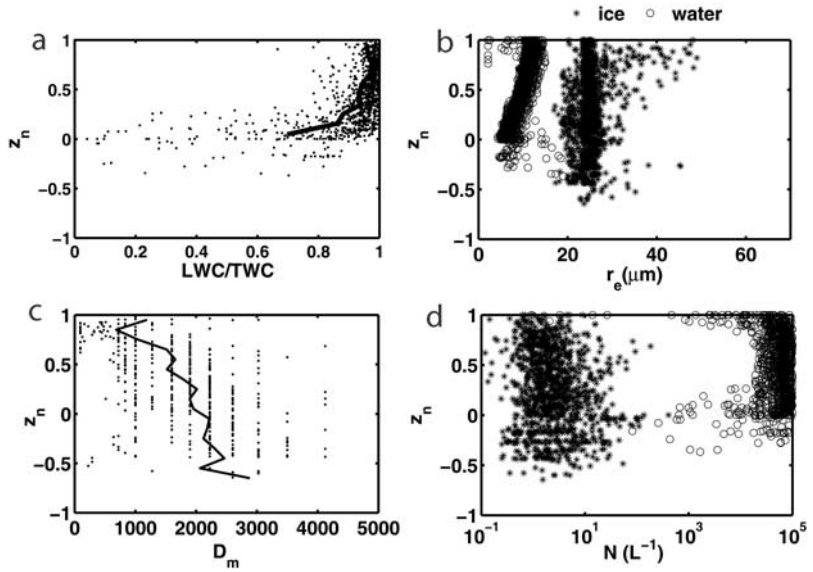

Figure 14. Variation of bulk microphysical parameters as function of z_n using same data shown in Figure 13 acquired in single-layer mixed-phase clouds sampled on 9 October, 10 October and 12 October. Plotted are (a) f_l, (b) r_{ew} and r_{ei}, (c) D_m, and (d) N_w and N_i as function of z_n.

Table 2. N_i, N_w, r_{ei}, r_{ew}, LWC, and TWC Averaged Over All Spirals Flown Through Single-Layer Mixed-Phase Clouds on 9 October, 10 October, and 12 October[a]

Date	LWC, g m^{-3}	IWC, gm^{-3}	r_{ew}, μm	r_{ei}, μm	N_w, x10^3 L^{-1}	N_i, L^{-1}
9 Oct	0.193 ± 0.131	0.025 ± 0.060	9.37 ± 2.23	25.48 ± 1.30	72.21 ± 34.37	5.62 ± 12.10
10 Oct (a)	0.174 ± 0.120	0.015 ± 0.032	9.04 ± 2.41	24.61 ± 2.35	25.74 ± 13.43	1.60 ± 2.40
10 Oct (b)	0.154 ± 0.116	0.006 ± 0.006	10.93 ± 2.57	25.76 ± 5.72	23.00 ± 9.97	2.04 ± 2.06
12 Oct	0.193 ± 0.116	0.006 ± 0.018	9.07 ± 2.29	25.15 ± 7.28	51.73 ± 16.60	2.07 ± 4.97

[a]Standard deviations correspond to deviations of the average value of each spiral from the average value integrated over all of the spirals.

Cober's [2004] analysis of FIRE ACE data. However, this work extends their results by showing the vertical dependence of f_l.

[40] Figure 14b shows the dependence of r_{ei} and r_{ew} on z_n. For the liquid drops, there is a clear increase of r_{ew} with z_n from a low value of 6.9 ± 1.8 μm for $0.0 < z_n < 0.1$ to a high value of 11.4 ± 2.4 μm for $0.9 < z_n < 1.0$. The dependence of r_{ew} on z_n can be roughly represented by

$$r_{ew} = 6.9 + 5.4 z_n \qquad [\mu\text{m}] \tag{6}$$

Increases in the average FSSP modal diameter from 10.2 μm to 24.1 μm (figure not shown) also occurred because of the condensational growth of supercooled drops throughout cloud and possibly because of collision-coalescence near cloud top where drizzle was sometimes detected. The FSSP measurements with nonzero r_{ew} at $z_n < 0.0$ (Figure 14b) correspond to where LWC > 0.0, which should be above z_n = 0.0 This ambiguity is mainly caused by an improperly identified cloud base due to an offset of the ground-based lidar from the spiral location or due to uncertainties in determining where the Citation descended below cloud base during ramped ascents and descents.

[41] Uncertainties in r_{ei} are larger than uncertainties in r_{ew}. Following *Fu* [1996], r_{ei} is proportional to the ratio of IWC to A_{ci}. Because the uncertainties in IWC are at least a factor of 2, especially when the HVPS data are missing, these translate into similar uncertainties in r_{ei}. Given that Appendix A shows that the IWC values from the SDs typically underestimate those from the CVI in ice-phase conditions, it is most likely that the r_{ei} in Figure 14b was underestimated. Higher-resolution observations of bulk mass contents, not available during M-PACE, would be required to reduce the uncertainties in r_{ei}. The small average r_{ei} values of 25.2 ± 3.9 μm are consistent with most of the ice mass being contained in hydrometeors with D > 1 mm (Figure 3): the mass-diameter relation $m = aD^b$ has an exponent of b = 1.7 meaning the ratio of IWC/A_c, that defines r_{ei} [*Fu*, 1996], actually decreases as particle size increases.

[42] The correlation of r_{ei} with z_n was only 0.25 compared to 0.72 for the correlation of r_{ew} with z_n. This lack of correlation of r_{ei} on z_n is consistent with observations of patches of ice occurring throughout cloud and represents average trends. There was a lot of variability between profiles. For some, like the spiral depicted in Figure 10, a trend of r_{ei} increasing with z_n was noted; similar behavior was seen on other profiles as seen for points corresponding to $z_n > 0.7$. The lack of dependence of r_{ei} on z_n is not necessarily inconsistent with the production of ice near tops of clouds from collision-coalescence and the continued growth during sedimentation by riming and condensation. Provided that the ratio of IWC/A_c remains constant, particles can grow without an increase in r_{ei} [*McFarquhar and Heymsfield*, 1998]. Figure 14c shows how the ice crystal median mass dimension, D_m varies with z_n. On average, D_m increased from 0.92 ± 0.70 mm at z_n of 0.8, to 1.9 ± 0.7 mm at z_n of 0.2, and to 2.3 ± 1.0 mm at z_n of −0.5 showing that ice particles indeed grew as they fell through the cloud and may have experienced growth due to aggregation below cloud base. This is consistent with the decrease in f_l with decreasing z_n illustrated in Figure 14a.

[43] Figure 14d shows how N_w and N_i varied as a function of z_n for the single-layer stratus. Because of uncertainties in measuring the concentrations of ice crystals with D < 53 μm, the N_i in ice-phase clouds only corresponds to particle sizes larger than those measured by the FSSP, namely D > 53 μm. Neither N_i nor N_w exhibited strong dependences on z_n, with correlations of 0.063 and 0.025 respectively. The N_i ranged between 10^{-1} L^{-1} and 10 L^{-1} with an average of 2.8 ± 6.9 L^{-1} and N_w ranged between 10^4 and 10^5 L^{-1} with an average of $44 \pm 31 \times 10^3$ L^{-1}. The standard deviations were larger than the averages because some very large N_i and N_w values occurred as seen in Figure 14d. On average, N_w changed by only 8% between z_n of 0.1 and 0.8 showing that the increase of the FSSP modal diameter and r_{ew} with z_n is explained through condensation and that additional nucleation did not take place inside the cloud. The decrease in the average N_w that occurs for $z_n > 0.8$ might be explained by either loss of droplets through collision-coalescence events or through cloud top entrainment.

[44] When including contributions from the FSSP in N_i for ice-phase conditions, the average N_i increased to 0.3 ± 1.8×10^3 L^{-1} with values as large as 32.4×10^3 L^{-1} noted during some spirals. The increase occurred because of the large concentrations of crystals with D < 53 μm measured by the FSSP in ice. Such large concentrations may not correspond to actual small crystal concentrations as the shattering of large ice crystals on protruding component of the FSSP may artificially enhance small crystal concentrations [e.g., *Field et al.*, 2006]. Because of uncertainties in determining ice crystal concentrations of D < 53 μm, Part 2 of this study [*Fridlind et al.*, 2007], compares measured and modeled ice crystal concentrations for D > 53 μm.

4.4. Summary of Vertical Variability Noted on Different Dates

[45] Table 2 summarizes the average and standard deviations of N_i, N_w, r_{ei}, r_{ew}, LWC and TWC observed for the 4 different days. Excluding the contributions of ice crystals

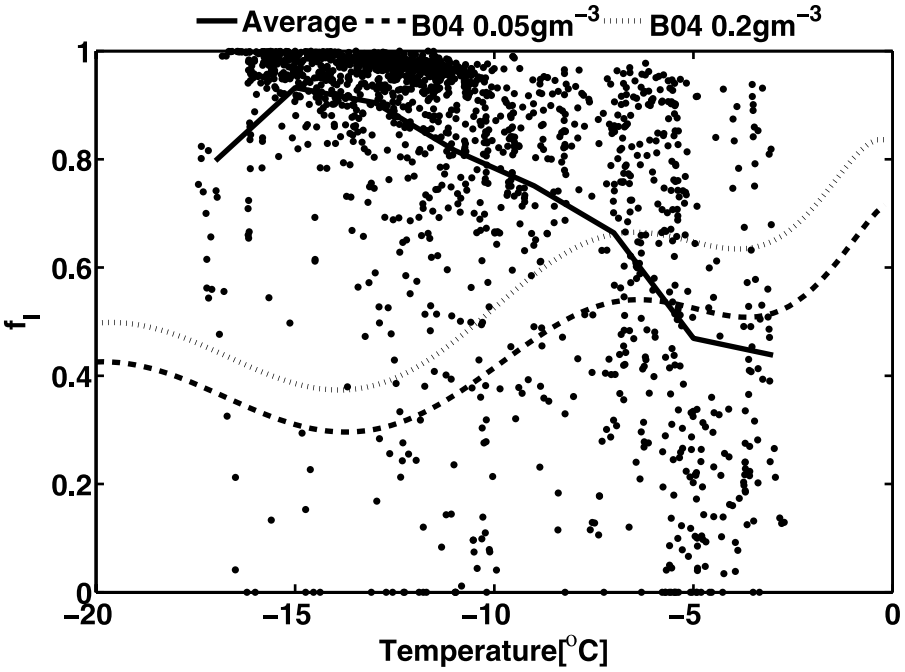

Figure 15. f_l derived from all 30-s averaged SDs in mixed-phase clouds obtained during profiles through single-layer Arctic stratus clouds on 9 October, 10 October and 12 October. Solid line represents average f_l as function of temperature. Dashed and dotted lines derived from parameterization scheme of *Boudala et al.* [2004] for TWCs of 0.05 and 0.2 g m^{-3}, respectively.

with $D < 53$ μm, the average N_i values range from a low value of 1.6 L^{-1} for the first spiral on 10 October to a high value of 5.6 L^{-1} for the spiral on 9 October. No strong correlation was noted between average N_i and N_w. However, the largest average N_w of 72×10^3 L^{-1} and the largest N_i of 5.6 L^{-1} were both recorded on 9 October, whereas lower N_w values of 26×10^3 and 23×10^3 L^{-1} and N_i values of 1.6 and 2.0 L^{-1} were recorded for the first and second flights on 10 October, respectively.

[46] These N_i are comparable to those previously measured in arctic mixed-phase stratus clouds. The observations obtained during M-PACE are similar to the Type V clouds identified by *Rangno and Hobbs* [2001]. These clouds contain larger droplets than the Type IV clouds of *Rangno and Hobbs* [2001] that are too thin or have too large concentrations to support the production of ice. Instead, in these Type V clouds the droplets attain larger sizes probably because the lower droplet concentrations are associated with a dearth of aerosols. This suggests that the higher concentrations of ice crystals may have formed from the fragmentation of delicate ice crystals and the freezing of drops. *Fridlind et al.* [2007] present a modeling study that explains these observations by analyzing model simulations that examine different processes that might explain the persistence of the mixed-phase clouds and the ice crystal production mechanisms.

5. Comparison With Past Observations of Mixed-Phase Clouds

[47] Prior observations of f_l as a function of TWC and temperature have provided a basis for developing large-scale model parameterizations and for evaluating the results of model simulations. Representations of f_l are also needed for continuous retrievals of cloud microphysical properties from ground-based remote sensors at ARM's NSA and other surface sites. Thus differences in how f_l varies as a function of TWC and temperature for M-PACE compared to other observations were characterized.

[48] Figure 15 shows f_l derived from M-PACE as a function of temperature where each point corresponds to a 30-s averaged SD from both the single-layer and multilayer stratus clouds. The solid line, representing the average f_l as a function of temperature, shows f_l increased with decreasing temperature. This occurs because the single-layer clouds all had a similar structure of a liquid-topped cloud with increasing fractions of cloud ice near cloud base and precipitating ice beneath. However, this relationship between f_l and temperature differs from conventional parameterization schemes [e.g., *Boudala et al.*, 2004] where f_l increases with increasing temperature. This shows that conventional parameterization schemes designed to represent the climatological properties of mixed-phase clouds in general are not applicable to the M-PACE observations. This has important implications for the representation of arctic boundary layer clouds in single-moment parameterization schemes for large-scale models and for the representation in remote sensing schemes that require fractions of liquid water content as input.

[49] Figure 16 shows the frequency distribution of f_l for all data measured in single-layer boundary clouds during M-PACE. Consistent with *McFarquhar and Cober*'s [2004] analysis of FIRE ACE arctic stratus clouds, the clouds are strongly dominated by the liquid droplets. This is also consistent with *Dong and Mace* [2003] and *Zuidema et al.*'s [2005] studies of arctic mixed-phase clouds and

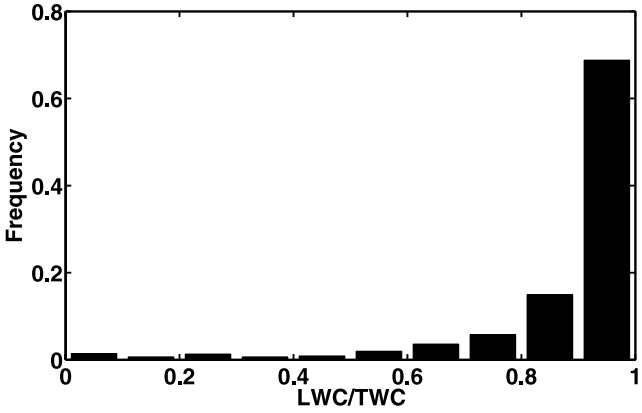

Figure 16. Normalized frequency distribution of f_l for all mixed-phase clouds sampled during profiles through single-layer Arctic stratus on 9 October, 10 October and 12 October.

Korolev et al. [2003] and *Cober et al.*'s [2001] studies of mixed-phase clouds in general. Previous studies have suggested that enhanced frequencies of f_l would also be noted for values in the range of 0.0 to 0.2, as there have been suggestions that few mixed-phase clouds have approximately equal amounts of water and ice, but rather are dominated by one or the other phase. The data presented in Figure 15 are not inconsistent with those conclusions. Data collected beneath cloud base in precipitating ice regions show f_l values near 0, corresponding to the exclusively ice clouds that must be present by mass continuity since most of the supercooled water must be glaciated at some stage before reaching the ground in the form of precipitation. Thus, although the results of this study are consistent with the results of previous studies, a significant dependence of the cloud microphysical quantities on the normalized cloud depth z_n has been developed which can have significant implications for both the longevity of mixed-phase clouds and the transfer of radiation.

6. Summary/Conclusions

[50] During M-PACE conducted over the North Slope of Alaska, the UND Citation was equipped with a full complement of cloud probes for measuring both the size-resolved and bulk properties of mixed-phase, ice-phase and liquid-phase clouds. During the 4-day period from 9 to 12 October, the UND Citation completed 53 vertical profiles through boundary layer arctic roll clouds in a single vertically continuous layer associated with a low-level northeasterly flow off of the pack ice that resulted in persistent low-level clouds under a sharp inversion [*Verlinde et al.*, 2007]. The cloud top heights over Oliktok Point and Barrow ranged from 837 to 1505 m and cloud top temperatures varied from $-10.8°$ to $-17.1°$C, well within the range where mixed-phase clouds might occur. Of the 513 30-s average cloud distributions measured during the 53 vertical profiles in single-layer clouds, 71% were collected in mixed-phase conditions, 23% in ice-phase and 6% in liquid-phase. These data represent the most complete set of mixed-phase cloud vertical profiles thus far obtained. The principal conclusions of the study are as follows:

[51] 1. Ice crystals with maximum dimension (D) > 1.3 mm contributed roughly 90% to the ice water content (IWC) of the mixed-phase clouds and hence need to be considered when calculating the bulk ice cloud properties.

[52] 2. For the single-layer mixed-phase clouds sampled, the liquid fraction f_l increased with normalized cloud altitude z_n, where $z_n = 1$ at cloud top and $z_n = 0$ at cloud base, representing liquid-topped clouds precipitating ice. The variation of f_l with z_n was expressed as $f_l = 0.727 + 0.677\ z_n - 0.443\ z_n^2$ for $0 < z_n < 1$.

[53] 3. Although IWC was larger on average near z_b, ice was noted to occur in patches throughout cloud depth with ice being detected near cloud top on some spirals.

[54] 4. The effective radius of the liquid water drops, r_{ew}, increased with z_n with the rate of increase represented by $r_{ew} = 6.9 + 5.4\ z_n$. The increase of r_{ew} with z_n was mainly attributed to condensational growth, with some evidence of collision-coalescence producing drizzle on some days since drizzle was detected in 18% of the mixed-phase observations.

[55] 5. The effective radius of ice crystals, r_{ei}, did not strongly depend on z_n with a correlation coefficient of 0.25. The average r_{ei} was 25.2 ± 3.9 μm. However, the median mass dimension, D_m increased with decreasing z_n from 0.9 ± 0.7 mm at z_n of 0.8, to 1.9 ± 0.7 mm at z_n of 0.2 and 2.3 ± 1.0 mm at z_n of -0.5.

[56] 6. The measured cloud droplet concentrations, N_w, averaged $43.6 \pm 30.5 \times 10^3$ L^{-1} and did not strongly depend on z_n. There were variations in N_w for the 4 different flights, with average values ranging from 23 to 72×10^3 L^{-1}.

[57] 7. Measured ice crystal concentrations for crystals with D > 53 μm, N_i, ranged from 1.6 to 5.6 L^{-1} on average for the 4 different flights, and averaged 2.8 ± 6.9 L^{-1} in total. For ice-phase conditions, when including the concentrations of crystals with D < 53 μm the average N_i increased to $0.3 \pm 1.8 \times 10^3$ L^{-1} compared to 2.8 ± 6.9 L^{-1} when not including the small crystals.

[58] 8. Compared to past parameterizations of mixed-phase clouds produced from observations of mixed-phase clouds in diverse geographic locations that show an increase of f_l with temperature, the M-PACE observations showed f_l decreased with temperature from $-3°$ to $-12°$C. This shows the need for different representations of arctic mixed-phase single-layer boundary clouds that have a strong structure of a liquid-topped cloud with precipitating ice below.

[59] Consistent with the study of *Lawson et al.* [2001], variability in both the horizontal and vertical structure of the mixed-phase clouds was noted. However, the common structure of liquid-topped clouds with precipitating ice below, previously seen by *Hobbs and Rangno* [1998], was consistently noted. Compared to *Rangno and Hobbs*'s [2001] observations of ice in arctic clouds, the M-PACE observations were comparable to their Type V clouds with droplet concentrations less than 100×10^3 L^{-1}, r_{ew} greater than 10 μm and ice crystal concentrations between 10 and 100 L^{-1}. Even if the number concentrations from the FSSP were not included in the total ice crystal concentrations, this suggests that the ice concentrations were at or above ice

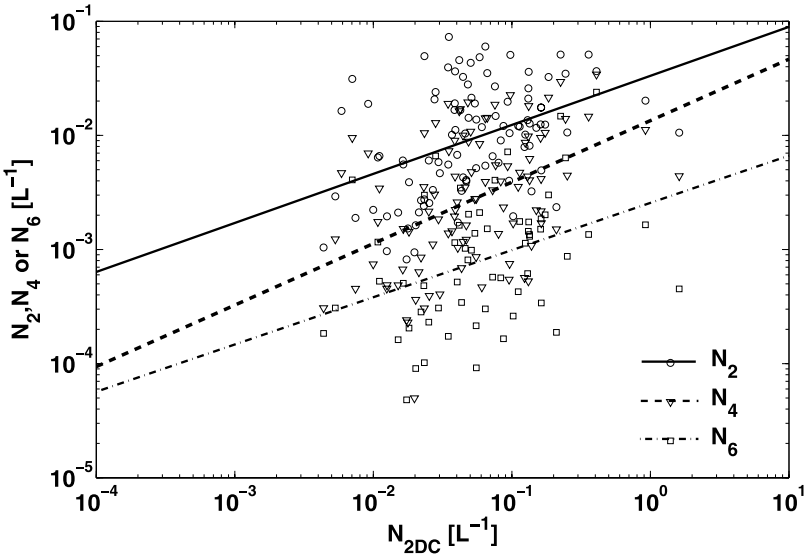

Figure A1. Relationship between N (D) for D = 2, 4 and 6 mm (N_2, N_4 and N_6) and total number concentration measured by the 2DC, N_{2DC}, for flights on 10 October (second flight) and 12 October when both the HVPS and 2DC recorded data. Each point represents 30 s average.

nucleus concentrations measured during M-PACE [*Prenni et al.*, 2007], hence suggesting that ice might have been generated by the fragmentation of crystals and the shattering of freezing drops [*Rangno and Hobbs*, 2001]. These in situ cloud observations, combined with the ground-based remote sensing observations and soundings obtained during M-PACE were also used in modeling studies to constrain possible mechanisms of ice formation that might explain the observations and to test various hypotheses related to the persistence of mixed-phase clouds. Part 2 [*Fridlind et al.*, 2007] uses the data presented here to investigate these issues.

[60] Future studies should also investigate whether the observations obtained in these single-layer boundary layer fall clouds are representative of arctic mixed-phase clouds in general. *Zhang et al.* [2006] examined the differences between the properties of the mixed-phase clouds that were observed to occur in multiple levels for flights conducted earlier in October 2004 during M-PACE. Future studies should also concentrate on making observations during the arctic springtime when the ambient flow brings anthropogenic pollutants to the Arctic from Asia and North America, potentially increasing the numbers of ice nuclei available that may affect the cloud properties.

Appendix A: Corrections to SDs to Account for Missing HVPS Data

[61] Figure 3 shows that particles with D > 1.3 mm contributed roughly 80% to the total mass estimated from the SD averaged over times on 12 October when both the 2DC and HVPS were working. Since particles with D > 1.3 mm dominated the IWC, they had to be accounted for when estimating IWC, and hence r_{ei}, from the SDs for flights on 9 and 10 October when the HVPS did not record data.

[62] Data from flights on 10 and 12 October, when the HVPS recorded data, were used to derive relationships between N(D) for D = 2, 4 and 6 mm (hereafter N_2, N_4 and N_6) and the total concentration measured by the 2DC, N_{2DC}. Figure A1 shows N_2, N_4 and N_6 as a function of N_{2DC}. Despite the scatter in Figure A1, relationships given by

$$\log_{10}\left(N(D=x)\right) = a_x + b_x \log_{10}\left(N_{2DC}\right) \tag{A1}$$

where (a_x, b_x) = (0.4276, −1.4784), (0.5387, −1.871) and (0.4138, −2.5909) for x = 2, 4 and 6 mm respectively, represent the data to some extent as the respective correlations were given by 0.4213, 0.4362 and 0.3723.

[63] For flights on 9 and 10 October without HVPS data, the measured N_{2DC} was thus used to estimate N_2, N_4, and N_6 for each 30 s time period. These three points, together with the SD measured by the 2DC, were then used to determine c_i and d_i that minimized the χ^2 difference with a logarithmic representation of the SD given by

$$\log(\mathrm{N(D)}) = \mathrm{c_i} + \mathrm{d_i} \log \mathrm{D}. \tag{A2}$$

It should be noted that this fit procedure gives N(D) for D > 1.3 mm most consistent with the HVPS observations and IWC observed by the CVI, and does not necessarily represent N(D) well for D < 1.3 mm. The N_2, N_4, and N_6 needed to be included in the fitting procedure to force the extrapolated SDs to match patterns observed with HVPS data.

[64] Although this fitting procedure was only used when the HVPS did not record data, its use is illustrated using the average size distribution measured on 10 October when both the 2DC and HVPS recorded data. This allows an assessment of the uncertainties associated with the extrapolation of the 2DC SDs to larger sizes. Figure A2 shows

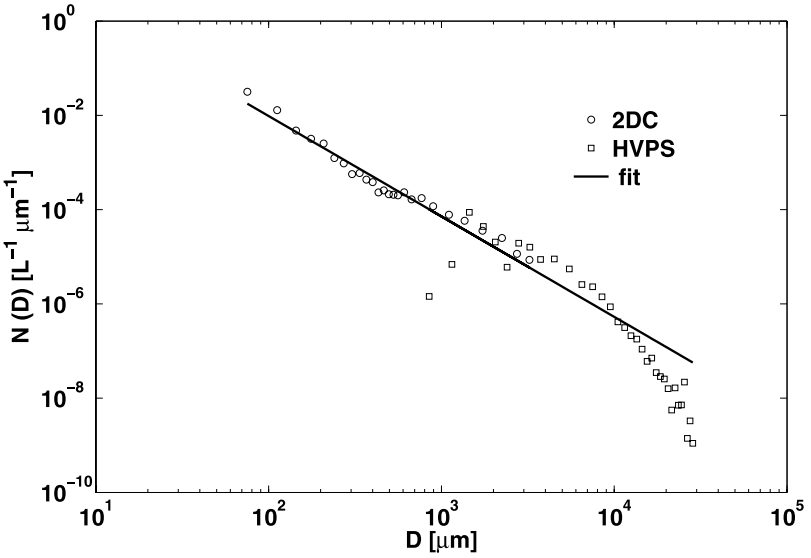

Figure A2. Average N(D) measured by 2DC and HVPS on 10 October (second flight) as function of D. Solid line represents best fit to data obtained using procedure outlined in Appendix A that does not take into account HVPS data.

the SDs measured by the 2DC and HVPS together with a fit to the data using the techniques above; the HVPS data were not used in the fitting procedure. The fit overestimates N(D) for D > 15 mm, but such particle sizes contributed at most about 10% to the total mass content. Given the absence of any data with D > 1.3 mm were used in the fitting procedure, the representations of the SDs are reasonable.

[65] To further assess the quality of the fit and to determine the accuracy with which bulk properties can be predicted from the observed SDs, the bulk masses derived from the 2DC and fit SDs were compared against those measured by the CVI. As discussed in section 3, the IWC was estimated from the SDs assuming the mass of an individual particle was given by $m = aD^b$ with the (a,b) coefficients selected for each day to minimize the difference between the CVI mass and than estimated from the SDs. Figure A3 compares the IWC computed from the SDs against that observed by the CVI for all 30 s periods when the cloud phase was identified as ice. The IWC from the measured/extrapolated SDs was biased high by an average factor of 0.85 compared to that measured by CVI probe, with a correlation coefficient of 0.5416. The IWC from the SDs were most noticeable overestimates for IWC < 0.01 g

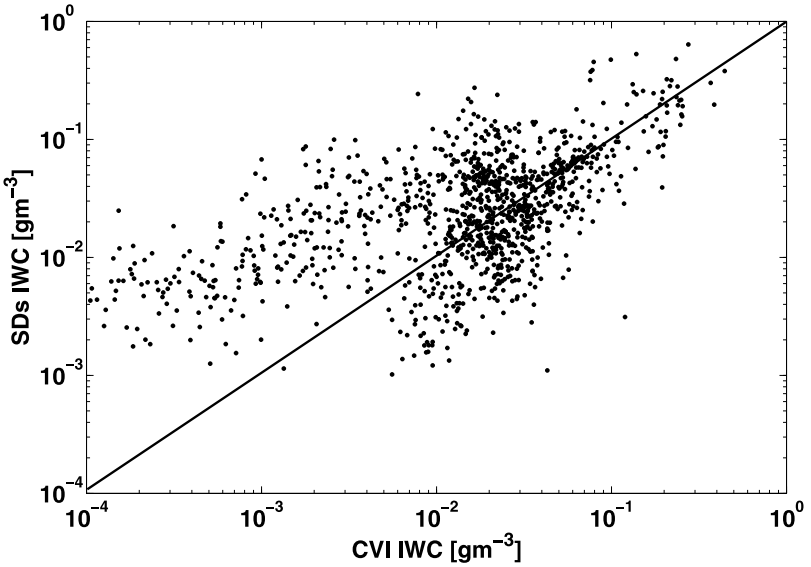

Figure A3. IWC estimated from 2DC SDs (D < 1300 μm) and fits (D > 1300 μm) versus IWC measured by CVI in ice-phase clouds. Data from all 30 s observations identified as ice-phase from single-layer clouds on 9 and 10 October (first spiral) are included in plot.

m^{-3}. Hence, although this technique was not ideal for extending the 2DC SDs to D > 1.3 mm and invoked additional uncertainties, there was no other reasonable alternative and the associated errors were reasonable.

[66] **Acknowledgments.** This research was sponsored by the Department of Energy Atmospheric Radiation Measurement Program (ARM) under contracts DE-FG03-02ER63337 and DE-FG02-07ER64378 and by the ARM Uninhabited Aerospace Vehicle (UAV) Program. Data were obtained from the ARM program archive, sponsored by DOE, Office of Science, Office of Biological and Environmental Research, Environmental Science Division. The dedication and efforts of the UND, ARM UAV and Scaled Composites field crews in the collection of a high-quality data set were appreciated. The collection of the M-PACE data would not have been possible without the initiative of J. Verlinde. The assistance of M. Freer in figure preparation was appreciated.

References

Baumgardner, D., and A. Korolev (1997), Airspeed corrections for optical array probe sample volumes, *J. Atmos. Oceanic Technol.*, *14*, 1224–1229.

Borovikov, A. M., L. I. Gaivoronskii, E. G. Zak, V. V. Kostarev, I. Z. Mazin, V. E. Minervin, A. K. Khrgian, and S. M. Shmeter (1963), *Cloud Physics*, 392 pp., Israel Program for Sci. Transl., Jerusalem, Israel.

Boudala, F. S., G. A. Isaac, Q. Fu, and S. G. Cober (2002), Parameterization of effective ice particle size for high-latitude clouds, *Int. J. Climatol.*, *22*, 1267–1284.

Boudala, F. S., G. A. Isaac, S. G. Cober, and Q. Fu (2004), Liquid fraction in stratiform mixed-phase clouds from in situ observations, *Q. J. R. Meteorol. Soc.*, *130*, 2919–2931.

Bower, K. N., S. J. Moss, D. W. Johnson, T. W. Choularton, J. Latham, P. R. A. Brown, A. M. Blyth, and J. Cardwell (1996), A parameterization of the ice water content observed in frontal and convective clouds, *Q. J. R. Meteorol. Soc.*, *122*, 1815–1844.

Brown, P. R. A., and P. N. Francis (1995), Improved measurements of ice water content in cirrus using a total-water probe, *J. Atmos. Oceanic Technol.*, *12*, 410–414.

Carrio, G. G., H. Jiang, and W. R. Cotton (2005), Impact of aerosol intrusions on Arctic boundary layer clouds. Part I: 4 May 1998 case, *J. Atmos. Sci.*, *62*, 3082–3093.

Cober, S. G., G. A. Isaac, A. V. Korolev, and J. W. Strapp (2001), Assessing cloud-phase conditions, *J. Appl. Meteorol.*, *40*, 1967–1983.

Curry, J. A., and E. E. Ebert (1992), Annual cycle of radiation fluxes over the Arctic Ocean: Sensitivity to cloud optical properties, *J. Clim.*, *5*, 1267–1280.

Curry, J. A., et al. (2000), FIRE Arctic Clouds Experiment, *Bull. Am. Meteorol. Soc.*, *81*, 5–29.

Dong, X., and G. G. Mace (2003), Arctic stratus cloud properties and radiative forcing derived from ground-based data collected at Barrow, Alaska, *J. Clim.*, *16*, 445–461.

Dong, X., G. G. Mace, P. Minnis, and D. F. Young (2001), Arctic stratus cloud properties and their effect on the surface radiation budget: Selected cases from FIRE ACE, *J. Geophys. Res.*, *106*, 15,297–15,312.

Ebert, E. E., and J. A. Curry (1993), An intermediate one-dimensional thermodynamic sea ice model for investigating ice-atmosphere interactions, *J. Geophys. Res.*, *98*, 10,085–10,110.

Feind, R. E., A. G. Detwiler, and P. L. Smith (2000), Cloud liquid water measurements on the armored T-29: Intercomparison between Johnson-Williams cloud water meter and CSIRO (King) liquid water probe, *J. Atmos. Oceanic Technol.*, *17*, 1630–1638.

Field, P. R., R. Wood, P. R. A. Brown, P. H. Kaye, E. Hirst, R. Greenaway, and J. A. Smith (2003), Ice particle inter-arrival times measured with a fast FSSP, *J. Atmos. Oceanic Technol.*, *20*, 249–261.

Field, P. R., R. J. Hogan, P. R. A. Brown, A. J. Illingworth, T. W. Choularton, P. H. Kaye, E. Hirst, and R. Greenaway (2004), Simultaneous radar and aircraft observations of mixed-phase cloud at the 100-m scale, *Q. J. R. Meteorol. Soc.*, *130*, 1877–1904.

Field, P. R., A. J. Heymsfield, and A. Bansemer (2006), Shattering and particle inter-arrival times measured by optical array probes in ice clouds, *J. Atmos. Oceanic Technol.*, *23*, 1357–1371.

Fleishauer, R. P., V. E. Larson, and T. H. Vonder Haar (2002), Observed microphysical structure of midlevel, mixed-phase clouds, *J. Atmos. Sci.*, *59*, 1779–1804.

Fridlind, A. M., A. S. Ackerman, G. M. McFarquhar, G. Zhang, M. R. Poellot, P. J. DeMott, A. J. Prenni, and A. J. Heymsfield (2007), Ice properties of single-layer stratocumulus during the Mixed-Phase Arctic Cloud Experiment: 2. Model results, *J. Geophys. Res.*, doi:10.1029/2007JD008646, in press.

Frisch, A. S., M. Shupe, I. Djalalova, G. Feingold, and M. Poellot (2002), The retrieval of stratus cloud droplet effective radius with cloud radars, *J. Atmos. Oceanic Technol.*, *19*, 835–842.

Fu, Q. (1996), An accurate parameterization of the solar radiative properties of cirrus clouds, *J. Clim.*, *9*, 2058–2082.

Gardiner, B. A., and J. Hallett (1985), Degradation of in-cloud forward scattering spectrometer probe measurements in the presence of ice particles, *J. Atmos. Oceanic Technol.*, *2*, 171–180.

Girard, E., and J. A. Curry (2001), Simulation of Arctic low-level clouds observed during the FIRE Arctic Clouds Experiment using a new bulk microphysics scheme, *J. Geophys. Res.*, *106*, 15,139–15,154.

Gregory, D., and D. Morris (1996), The sensitivity of climate simulations to the specification of mixed phase clouds, *Clim. Dyn.*, *12*, 641–651.

Hallett, J. (2003), Measurement in the atmosphere, in *Handbook of Weather, Climate and Water: Dynamics, Climate, Physical Meteorology, Weather Systems and Measurements*, edited by T. D. Potter and B. R. Colman, pp. 711–720, John Wiley Hoboken, N. J.

Harrington, J. Y., and P. Q. Olsson (2001), On the potential influence of ice nuclei on surface-forced marine stratocumulus cloud dynamics, *J. Geophys. Res.*, *106*, 27,473–27,484.

Harrington, J. Y., T. Reisin, W. R. Cotton, and S. M. Kreidenweis (1999), Cloud resolving simulations of Arctic stratus. Part II: Transition-season clouds, *Atmos. Res.*, *51*, 45–75.

Heymsfield, A. J. (1993), Microphysical structures of stratiform and cirrus clouds, in *Aerosol-Cloud-Climate Interactions*, edited by P. V. Hobbs, pp. 97–121, Elsevier, New York.

Heymsfield, A. J., and J. L. Parrish (1978), A computational technique for increasing the effective sampling volume of the PMS two-dimensional particle size spectrometer, *J. Appl. Meteorol.*, *17*, 1566–1572.

Heymsfield, A. J., S. Lewis, A. Bansemer, J. Iaquinta, L. M. Miloshevich, M. Kajikawa, C. Twohy, and M. R. Poellot (2002), A general approach for deriving the properties of cirrus and stratiform ice cloud properties, *J. Atmos. Sci.*, *59*, 3–29.

Hobbs, P. V., and A. L. Rangno (1998), Microstructures of low and middle-level clouds over the Beaufort Sea, *Q. J. R. Meteorol. Soc.*, *124*, 2035–2071.

Hobbs, P. V., A. L. Rangno, M. Shupe, and T. Uttal (2001), Airborne studies of cloud structures over the Arctic Ocean and comparisons with retrievals from ship-based remote sensing observations, *J. Geophys. Res.*, *106*, 15,029–15,044.

Hogan, R. J., M. P. Mittermaier, and A. J. Illingworth (2006), The retrieval of ice water content from radar reflectivity factor and temperature and its use in evaluating a mesoscale model, *J. Appl. Meteorol. Clim.*, *45*, 301–317.

Intrieri, J. M., M. D. Shupe, T. Uttal, and B. J. McCarty (2002a), An annual cycle of Arctic cloud characteristics observed by radar and lidar at SHEBA, *J. Geophys. Res.*, *107*(C10), 8030, doi:10.1029/2000JC000423.

Intrieri, J. M., C. W. Fairall, M. D. Shupe, P. O. G. Persson, E. L. Andreas, P. S. Guest, and R. E. Moritz (2002b), An annual cycle of Arctic surface cloud forcing at SHEBA, *J. Geophys. Res.*, *107*(C10), 8039, doi:10.1029/2000JC000439.

Jiang, H., W. R. Cotton, J. O. Pinto, J. A. Curry, and M. J. Weissbluth (2000), Cloud resolving simulations of mixed-phase Arctic stratus observed during BASE: Sensitivity to concentration of ice crystals and large-scale heat and moisture advection, *J. Atmos. Sci.*, *57*, 2105–2117.

Khvorostyanov, V. I., J. A. Curry, J. O. Pinto, M. Shupe, B. A. Baker, and K. Sassen (2001), Modeling with explicit spectral water and ice microphysics of a two-layer cloud system of altostratus and cirrus observed during the FIRE Arctic Clouds Experiment, *J. Geophys. Res.*, *106*, 15,099–15,112.

King, W. D., J. E. Dye, D. Baumgardner, J. W. Strapp, and D. Huffman (1985), Icing wind tunnel tests on the CSIRO liquid water probe, *J. Atmos. Oceanic Technol*, *2*, 340–352.

Korolev, A. V., G. A. Isaac, and J. Hallett (1999), Ice particle habits in Arctic clouds, *Geophys. Res. Lett.*, *26*, 1299–1302.

Korolev, A., G. A. Isaac, S. G. Cober, J. W. Strapp, and J. Hallett (2003), Microphysical characterization of mixed-phase clouds, *Q. J. R. Meteorol. Soc.*, *129*, 39–65.

Lane, D. E., J. O. Pinto, and J. A. Curry (2001), Evaluation of GCM radiation codes using SHEBA data, in *Sixth Conference on Polar Meteorology and Oceanography*, pp. 285–288, Am. Meteorol. Soc., San Diego, Calif.

Lawson, R., B. A. Baker, C. G. Schmitt, and T. L. Jensen (2001), An overview of microphysical properties of Arctic clouds observed in May and July 1998 during FIRE ACE, *J. Geophys. Res.*, *106*, 14,989–15,014.

Li, Z.-X., and H. Le Treut (1992), Cloud-radiation feedbacks in a general circulation model and their dependence on cloud modeling assumptions, *Clim. Dyn.*, *7*, 133–139.

Locatelli, J. D., and P. V. Hobbs (1974), Fall speeds and masses of solid precipitation particles, *J. Geophys. Res.*, *79*, 2185–2197.

Lohmann, U. (2002), A glaciation indirect effect caused by soot aerosols, *Geophys. Res. Lett.*, *29*(4), 1052, doi:10.1029/2001GL014357.

McFarquhar, G. M., and S. G. Cober (2004), Single-scattering properties of mixed-phase Arctic clouds at solar wavelengths: Impacts on radiative transfer, *J. Clim.*, *17*, 3799–3813.

McFarquhar, G. M., and A. J. Heymsfield (1996), Microphysical characteristics of three cirrus anvils sampled during the Central Equatorial Pacific Experiment (CEPEX), *J. Atmos. Sci.*, *53*, 2401–2423.

McFarquhar, G. M., and A. J. Heymsfield (1998), The definition and significance of an effective radius for ice clouds, *J. Atmos. Sci.*, *55*, 2039–2052.

McFarquhar, G. M., S. Iacobellis, and R. C. J. Somerville (2003), SCM simulations of tropical ice clouds using observationally based parameterizations of microphysics, *J. Clim.*, *11*, 1643–1664.

McFarquhar, G. M., M. S. Timlin, R. M. Rauber, B. F. Jewett, J. A. Grim, and D. P. Jorgensen (2007a), Vertical variability of cloud hydrometeors in the stratiform region of mesoscale convective systems and bow echoes, *Mon. Weather Rev.*, *135*, 3405–3428.

McFarquhar, G. M., J. Um, M. Freer, D. Baumgardner, G. L. Kok, and G. Mace (2007b), Importance of small ice crystals to cirrus properties: Observations from the Tropical Warm Pool International Cloud Experiment (TWP-ICE), *Geophys. Res. Lett.*, *34*, L13803, doi:10.1029/2007GL029865.

Mitchell, D. L. (1996), Use of mass- and area-dimensional power laws for determining precipitation particle terminal velocities, *J. Atmos. Sci.*, *53*, 1710–1723.

Morrison, H., M. D. Shupe, and J. A. Curry (2003), Modeling clouds observed at SHEBA using a bulk microphysics parameterization implemented into a single-column model, *J. Geophys. Res.*, *108*(D8), 4255, doi:10.1029/2002JD002229.

Morrison, H., J. A. Curry, and V. I. Khvorostyanov (2005a), A new double-moment microphysics scheme for application in cloud and climate models. Part I: Description, *J. Atmos. Sci.*, *62*, 1665–1677.

Morrison, H., J. A. Curry, M. D. Shupe, and P. Zuidema (2005b), A new double-moment microphysics parameterization for application in cloud and climate models. Part II: Single-column modeling of Arctic clouds, *J. Atmos. Sci.*, *62*, 1678–1693.

Moss, S. J., and D. W. Johnson (1994), Aircraft measurements to validate and improve numerical model parameterizations of ice to water ratios in clouds, *Atmos. Res.*, *34*, 1–25.

Nousiainen, T., and G. M. McFarquhar (2004), Radiative properties of small quasi-spherical ice crystals, *J. Atmos. Sci.*, *61*, 2229–2248.

Pinto, J. O. (1998), Autumnal mixed-phase cloudy boundary layers in the Arctic, *J. Atmos. Sci.*, *55*, 2016–2038.

Platnick, S., J. Y. Li, M. D. King, H. Gerber, and P. V. Hobbs (2001), A solar reflectance method for retrieving the optical thickness and droplet size of liquid water clouds over snow and ice surfaces, *J. Geophys. Res.*, *106*, 15,185–15,200.

Poellot, M. R., and D. Brown (2006), A case study of horizontal variability in Arctic cloud microphysical properties, paper presented at 16th Atmospheric Radiation Measurement (ARM) Science Team Meeting, Atmos. Radiat. Meas. Program, U.S. Dep. of Energy, Albuquerque, N. M. (Available at http://www.arm.gov/publications/proceedings/conf16/extended_abs/poellot_m.pdf)

Prenni, A. J., J. Y. Harrington, M. Tjernström, P. J. DeMott, A. Avramov, C. N. Long, S. M. Kreidenweis, P. Q. Olsson, and J. Verlinde (2007), Can ice-nucleating aerosols affect arctic seasonal climate?, *Bull. Am. Meteorol. Soc.*, *88*, 541–550.

Rangno, A., and P. Hobbs (2001), Ice particles in stratiform clouds in the Arctic and possible mechanisms for the production of high ice concentrations, *J. Geophys. Res.*, *106*, 15,065–15,075.

Rotstayn, L. D., B. F. Ryan, and J. J. Katzfey (2000), A scheme for calculation of the liquid fraction in mixed-phase stratiform clouds in large-scale models, *Mon. Weather Rev.*, *128*, 1070–1088.

Shupe, M. D., T. Uttal, S. Matrosov, and A. S. Frisch (2001), Cloud water contents and hydrometeor sizes during the FIRE Arctic Clouds Experiment, *J. Geophys. Res.*, *106*, 15,015–15,028.

Shupe, M. D., S. Y. Matrosov, and T. Uttal (2005), Arctic mixed-phase cloud properties derived from surface-based sensors, paper presented at 15th Atmospheric Radiation Measurement (ARM) Science Team Meeting, Atmos. Radiat. Meas. Program, U.S. Dep. of Energy, Daytona Beach, Fla. (Available at http://www.arm.gov/publications/proceedings/conf15/extended_abs/shupe_md.pdf)

Smith, R. N. B. (1990), A scheme for predicting layer clouds and their water content in a general circulation model, *Q. J. R. Meteorol. Soc.*, *116*, 435–460.

Strapp, J. W., F. Albers, A. Reuter, A. V. Korolev, U. Maixner, E. Rashke, and Z. Vukovic (2001), Laboratory measurements of the response of a PMS OAP-2DC, *J. Atmos. Oceanic Technol.*, *18*, 1150–1170.

Strapp, J. W., J. Oldenburg, R. Ide, L. Lilie, S. Bacic, Z. Vukovic, M. Oleskiw, D. Miller, E. Emergy, and G. Leone (2003), Wind tunnel measurements of the response of hot-wire liquid water content instruments to large droplets, *J. Atmos. Oceanic Technol.*, *20*, 791–806.

Sun, Z., and K. P. Shine (1994), Studies of the radiative properties of ice and mixed-phase clouds, *Q. J. R. Meteorol. Soc.*, *120*, 111–137.

Tsay, S.-C., and K. Jayaweera (1984), Physical characteristics of Arctic stratus clouds, *J. Clim. Appl. Meteorol.*, *23*, 584–596.

Twohy, C. H., J. W. Strapp, and M. Wendisch (2003), Performance of a Counterflow Virtual Impactor in the NASA Icing Research Tunnel, *J. Atmos. Oceanic Technol.*, *20*, 781–790.

Verlinde, J., et al. (2007), The Mixed-Phase Arctic Cloud Experiment, *Bull. Am. Meteorol. Soc.*, *88*, 205–221.

Vorosmarty, C., L. Hinzman, B. Peterson, D. Bromwich, L. Hamilton, J. Morison, V. Romanovsky, M. Sturm, and R. Webb (2002), Arctic-CHAMP: A program to study Arctic hydrology and its role in global climate, *EOS Trans. AGU*, *83*, 241, 244–245, 249.

Walsh, J. E., and W. L. Chapman (1998), Arctic cloud-radiation-temperature associations in observational data and atmospheric reanalyses, *J. Clim.*, *11*, 3030–3045.

Wang, Z., and K. Sassen (2001), Cloud type and macrophysical property retrieval using multiple remote sensors, *J. Appl. Meteorol.*, *41*, 218–229.

Wang, Z., K. Sassen, D. Whiteman, and B. Demoz (2005), The analysis of multi-year low-level and mid-level mixed-phase clouds observed at the North Slope of Alaska Cloud and Radiation Testbed site, paper presented at 15th Atmospheric Radiation Measurement (ARM) Science Team Meeting, Atmos. Radiat. Meas. Program, U.S. Dep. of Energy, Daytona Beach, Fla.

Zhang, G., G. M. McFarquhar, J. Verlinde, M. Poellot, and A. Heymsfield (2006), Contrasting properties of single-layer and multi-layer Arctic stratus sampled during the Mixed-Phase Arctic Cloud Experiment, paper presented at 16th Atmospheric Radiation Measurement (ARM) Science Team Meeting, Atmos. Radiat. Meas. Program, U.S. Dep. of Energy, Albuquerque, N. M. (Available at http://www.arm.gov/publications/proceedings/conf16/extended_abs/zhang_g.pdf)

Zhang, T., K. Stamnes, and S. A. Bowling (1996), Impact of clouds on surface radiative fluxes and snowmelt in the Arctic and subarctic, *J. Clim.*, *9*, 2110–2123.

Zuidema, P., B. Baker, Y. Han, J. Intrieri, J. Key, P. Lawson, S. Matrosov, M. Shupe, R. Stone, and T. Uttal (2005), An Arctic springtime mixed-phase cloudy boundary layer observed during SHEBA, *J. Atmos. Sci.*, *62*, 160–176.

A. Fridlind, NASA Goddard Institute for Space Studies, New York, NY 10025, USA.

A. J. Heymsfield, National Center for Atmospheric Research, Boulder, CO 80307, USA.

G. L. Kok, Droplet Measurement Technologies, Boulder, CO 80301, USA.

R. McCoy and T. Tooman, Sandia National Laboratories, Livermore, CA 94551, USA.

G. M. McFarquhar and G. Zhang, Department of Atmospheric Sciences, University of Illinois, 105 S. Gregory Street, Urbana, IL 61801, USA. (mcfarq@atmos.uiuc.edu)

M. R. Poellot, Department of Atmospheric Sciences, University of North Dakota, Grand Forks, ND 58202, USA.